

ARMY RESEARCH LABORATORY



Optimization of PZT Thin Film Crystalline Orientation Through Optimization of TiO₂/Pt Templates

by Daniel M. Potrepka, Glen R. Fox, and Ronald G. Polcawich

ARL-TR-5431

January 2011

NOTICES

Disclaimers

The findings in this report are not to be construed as an official Department of the Army position unless so designated by other authorized documents.

Citation of manufacturer's or trade names does not constitute an official endorsement or approval of the use thereof.

Destroy this report when it is no longer needed. Do not return it to the originator.

Army Research Laboratory

Adelphi, MD 20783-1197

ARL-TR-5431

January 2011

Optimization of PZT Thin Film Crystalline Orientation Through Optimization of TiO₂/Pt Templates

Daniel M. Potrepka and Ronald G. Polcawich
Sensors and Electron Devices Directorate, ARL

Glen R. Fox
Fox Materials Consulting LLC
7145 Baker Road, Colorado Springs, Colorado 80908

REPORT DOCUMENTATION PAGE

*Form Approved
OMB No. 0704-0188*

Public reporting burden for this collection of information is estimated to average 1 hour per response, including the time for reviewing instructions, searching existing data sources, gathering and maintaining the data needed, and completing and reviewing the collection information. Send comments regarding this burden estimate or any other aspect of this collection of information, including suggestions for reducing the burden, to Department of Defense, Washington Headquarters Services, Directorate for Information Operations and Reports (0704-0188), 1215 Jefferson Davis Highway, Suite 1204, Arlington, VA 22202-4302. Respondents should be aware that notwithstanding any other provision of law, no person shall be subject to any penalty for failing to comply with a collection of information if it does not display a currently valid OMB control number.

PLEASE DO NOT RETURN YOUR FORM TO THE ABOVE ADDRESS.

1. REPORT DATE (DD-MM-YYYY)	2. REPORT TYPE		3. DATES COVERED (From - To)		
January 2011	Summary		January 2009 to September 2010		
4. TITLE AND SUBTITLE			5a. CONTRACT NUMBER		
Optimization of PZT Thin Film Crystalline Orientation Through Optimization of TiO ₂ /Pt Templates			5b. GRANT NUMBER		
			5c. PROGRAM ELEMENT NUMBER		
			5d. PROJECT NUMBER		
6. AUTHOR(S)			5e. TASK NUMBER		
Daniel M. Potrepka, Glen R. Fox, and Ronald G. Polcawich			5f. WORK UNIT NUMBER		
7. PERFORMING ORGANIZATION NAME(S) AND ADDRESS(ES)			8. PERFORMING ORGANIZATION REPORT NUMBER		
U.S. Army Research Laboratory ATTN: RDRL-SER-L 2800 Powder Mill Road Adelphi, MD 20783-1197			ARL-TR-5431		
9. SPONSORING/MONITORING AGENCY NAME(S) AND ADDRESS(ES)			10. SPONSOR/MONITOR'S ACRONYM(S)		
			11. SPONSOR/MONITOR'S REPORT NUMBER(S)		
12. DISTRIBUTION/AVAILABILITY STATEMENT Approved for public release; distribution unlimited.					
13. SUPPLEMENTARY NOTES					
14. ABSTRACT <p>Titanium dioxide (TiO₂) seed/adhesion layers were produced by sputter depositing 15–45-nm thick Ti films on thermally grown silicon oxide (SiO₂) using a range of deposition conditions including deposition time, cathode power, and argon (Ar) gas pressure gas flow. The Ti films were oxidized and converted to the rutile TiO₂ phase by annealing in a tube furnace and were characterized by X-ray diffraction and ellipsometry. A 100-nm platinum (Pt) electrode layer was then sputter-deposited at 500 °C onto the TiO₂ seed layer. The Pt {111} orientation templates from the underlying {100} textured TiO₂ film, which forms during oxidation of the {0002} textured Ti film. Analysis of the 222 Pt X-ray diffraction peak shows an 8-fold improvement in peak height and a decrease in rocking curve full-width-at-half-maximum (FWHM) from 9° to 2° for the Pt deposited on an approximately 30 nm TiO₂ template compared to the same Pt process used for deposition onto a Ti template. Use of the Pt/TiO₂ electrode for growth of PZT(52/48) results in films with 90% textured volume fraction, which is expected to improve electrical properties of the PZT films.</p>					
15. SUBJECT TERMS Sputter film, Pt, titanium dioxide, crystal, X-ray diffraction, resistance, thickness					
16. SECURITY CLASSIFICATION OF:		17. LIMITATION OF ABSTRACT	18. NUMBER OF PAGES	19a. NAME OF RESPONSIBLE PERSON Daniel M. Potrepka	
a. REPORT Unclassified	b. ABSTRACT Unclassified	c. THIS PAGE Unclassified	UU	58	19b. TELEPHONE NUMBER (Include area code) (301) 394-0389

Contents

List of Figures	iv
List of Tables	v
Acknowledgment	vii
1. Introduction	1
2. Experimental Procedures	3
2.1 Materials and Processing Description	3
2.2 Thin Film Sheet Resistance Characterization Procedures	9
2.3 Thin Film Thickness and Refractive Index Characterization Procedures	11
2.4 Crystallinity Characterization Procedures	12
2.5 Rigaku Diffractometer Setup and Calibration Check.....	12
2.6 Measurement Procedure for Ti, TiO ₂ , Pt and PZT Thin Films	13
3. Results and Discussion	15
3.1 Ti Deposition and Effect of Sputtering Conditions	15
3.2 Ti, and TiO ₂ Thin Film Crystallography	27
3.3 Pt Thin Film Crystallography and Effect of TiO ₂ Seed Layer	31
4. Conclusion	37
5. References	38
Appendix A. Rigaku Diffractometer Setup & XRD SPC for TiO₂ Adhesion Layer	39
Appendix B. Currently-defined Process Recipe	43
Appendix C. Pt module for MEMS Exchange	45
List of Symbols, Abbreviations, and Acronyms	46
Distribution List	47

List of Figures

Figure 1. Sequence of layers composing the substrate and bottom electrode for PZT thin film growth.....	3
Figure 2. Positions for Ti thin film sheet resistance measurements with 4-point probe.....	10
Figure 3. Positions for Pt thin film sheet resistance measurements with 4-point probe.....	10
Figure 4. Positions for ellipsometry measurements of SiO ₂ and TiO ₂ coatings.....	11
Figure 5. Five-site sheet resistance as a function of wafer number and deposition order for Ti deposited on Matrix #1 wafers.....	15
Figure 6. Five-site sheet resistance as a function of cumulative sputter time for Ti deposited on Matrix #1 wafers.....	16
Figure 7. Five-site sheet resistance as a function of Ar flow rate (pressure) for Ti deposited on Matrix #2 wafers. The 0.16 Ohm/sq/sccm increase in sheet resistance with flow rate is due to a reduction in Ti deposition rate.	18
Figure 8. Average five-site sheet resistance measurement for 24 wafers deposited at the same fixed conditions of 1,000 W/30 sccm Ar/19 s from Ti Matrix #4. The decrease in sheet resistance for wafer #16 (with sputter time of 1261 s) results from a wafer positioning problem and possibly some other unidentified process variable.	19
Figure 9. Composite plot of sheet resistance values for wafers deposited in Ti Matrix #1, 2, and 4. Wafers deposited at the same fixed conditions of 1,000 W/30 sccm Ar/19 s should exhibit sheet resistance values within the upper and lower limit lines.	20
Figure 10. Ti Matrix #3 film R _s dependence on cathode power for fixed deposition times of 19 s and 95 s and a fixed Ar flow rate of 30 sccm.....	21
Figure 11. Ti Matrix #3 film 1/R _s dependence on cathode power for fixed deposition times of 19 s and 95 s and a fixed Ar flow rate of 30 sccm. Linear regression fit equations provide for calculation of R _s for SPC adjustments.	22
Figure 12. Ti film linear 1/R _s dependence on deposition time for fixed cathode powers of 500 W and 1,000 W and a fixed Ar flow rate of 30 sccm. Data is taken from Ti film Matrix #6.....	23
Figure 13. TiO ₂ thickness dependence on deposition time at 500 W/30 sccm Ar and 1,000 W/30 sccm Ar with 700 °C/15 min post anneal. Data from three wafers are plotted for each deposition time.....	23
Figure 14. Dependence of 1/R _s on Ti thickness for Matrix #6 wafers deposited at 500 W/30 sccm Ar and 1,000 W/30 sccm Ar.....	24
Figure 15. Dependence of resistivity on Ti thickness for Matrix #6 wafers deposited at 500 W/30 sccm Ar and 1,000 W/30 sccm Ar.	25
Figure 16. Ti R _s dependence on chamber history for Matrix #5 wafers deposited at 1,000 W/30 sccm Ar/19 s on three different days.	26

Figure 17. Ti R _s dependence on chamber history for Matrix #5 wafers deposited at 1,000 W/30 sccm Ar/19 s on three different days.....	26
Figure 18. XRD θ-2θ scan of an as-deposited Ti film confirming {0001}-texture.....	28
Figure 19. XRD θ-2θ scan of TiO ₂ film confirming {100} textured rutile structure and comparison with as deposited {0001} texture Ti film. The Ti and TiO ₂ film details are given for the Matrix #4/Wafer 21 sample for which the XRD pattern is displayed in red.....	29
Figure 20. Comparison of the 200 rutile XRD peak positions and intensities for TiO ₂ films formed by oxidation annealing between 650 and 800 °C.....	30
Figure 21. Comparison of the 200 rutile XRD peak FWHM for TiO ₂ films formed by oxidation annealing between 650 and 800 °C.....	30
Figure 22. TiO ₂ Rocking-curve FWHM dependence on anneal temperature and time.....	30
Figure 23. Comparison of the 200 rutile XRD peak positions, intensities, and FWHM for TiO ₂ films 20–42.5 nm thick deposited at 500 or 1,000 W.....	32
Figure 24. TiO ₂ Rocking Curve FWHM and position dependence on deposition thickness and RF power.....	32
Figure 25. Comparison of XRD θ–2θ spectrum for {111}-textured Pt, {100}-textured TiO ₂ seed layer and as-deposited {0001}-textured Ti film.....	33
Figure 26. Correlation of Intensity and FOM XRD for Pt vs. TiO ₂	34
Figure 27. Extended thickness range of Pt(222) XRD for peak intensity, peak FWHM, and rocking-curve FWHM.....	35
Figure 28. Comparison of Pt(111) process (#2) to prior ARL (#1) and NIST (#3 & #4) processes.....	36
Figure 29. Comparison of XRD θ-2θ spectrum for {111}-textured Pt, {100}-textured TiO ₂ seed layer and highly {111} textured PZT.....	36

List of Tables

Table 1. Ti deposition matrix #1 with varying presputter time for evaluation of Ti deposition stability over time (targeted thicknesses = 20 nm and 100 nm and actual thicknesses = 32 nm and 160 nm for the 19 s and 95 s depositions, respectively). The fourth wafer in each split, coated using a sputter time of 95 s, could be used as a PCM for thickness and sheet resistance measurements.....	4
Table 2. Ti deposition matrix #2 with varying Ar flow for evaluation of change in Ti deposition rate and properties with Ar flow and corresponding deposition pressure.....	5
Table 3. Ti deposition matrix #3 with varying applied cathode power for evaluation of change in Ti deposition rate and properties with deposition power.....	6
Table 4. Ti deposition matrix #4 with fixed deposition conditions for evaluation of change in Ti deposition stability and preparation of wafers for oxidation anneal experiments.....	7

Table 5. Ti deposition matrix #5 with fixed deposition conditions for evaluation of change in Ti deposition stability over time and the effect of substrate vender.	8
Table 6. Ti deposition matrix #6 with varying deposition time and power to obtain Ti thickness between 10 nm and 45 nm for evaluation of Ti, TiO ₂ and Pt properties.	9
Table 7. SiO ₂ and TiO ₂ ellipsometry measurements.	11
Table 8. Alumina CuK α_1 peak position, intensity and measurement ranges used for diffractometer calibration check.	13
Table 9. Summary of sheet resistance measurements and 3 σ limits determined from Matrix #1 for SPC of Ti films deposited at 1,000 W/30 sccm Ar.	17
Table 10. Summary of R _s dependence on cathode power, Ar flow rate and deposition time. Slope values can be used to correct deposition conditions to maintain deposition with UL and LL SPC limits.....	24

Acknowledgment

The authors wish to acknowledge Joel L. Martin (ARL) for his contributions to the processing of wafers used in this study.

INTENTIONALLY LEFT BLANK.

1. Introduction

A wide variety of the physical properties of materials, such as ferroelectricity, ferromagnetism, piezoelectricity, conductivity, and dielectric permittivity are anisotropic and are, therefore, strongly affected by crystallographic texture (1). With the appropriate choice of thin film texture, device operating efficiency and reliability can be strongly affected. Consequently, texture control is a critical factor for thin film process control and is fundamental to device reproducibility. This report on deposition and characterization of titanium dioxide (TiO_2) and platinum (Pt) thin film electrodes leverages the electrode developments reported for Ferroelectric Random Access Memory (FRAM) for application to Lead Zirconate Titanate ($\text{PbZr}_x\text{Ti}_{1-x}\text{O}_3$)-Microelectromechanical Systems (PZT-MEMS) device fabrication.

Because the Pt electrode crystallographic texture acts as a template for PZT film growth, the properties of ferroelectric PZT films can be degraded by uncontrolled Pt bottom electrode texture. In addition, factors such as bottom electrode film density, thickness, and grain size affect PZT film properties. Similarly Pt top electrode factors such as etch damage and thermal processing, in addition to the factors listed for the bottom electrode, influence PZT ferroelectric performance. Academic publications rarely describe the details for controlling the Pt texture and density, but a patented process has been reported for a bottom electrode consisting of 200 TiO_2 /111 Pt (2–4), which resulted in improved PZT ferroelectric capacitor electrical characteristics for FRAM applications. It is hypothesized that the improved PZT properties result from a reduction in lead loss by suppressed diffusion away from the PZT/Pt interface, as well as templating of the PZT crystal growth from the Pt {111} lattice, thus providing enhanced and reproducible {111} texture in the PZT.

Bottom electrodes for PZT capacitors can be fabricated from a variety of films such as Pt, iridium (Ir), IrO_2 , RuO_2 , and palladium (Pd), as well as other noble metals and conductive oxides (2–4). Currently, only Pt and Ir are used in mass-produced PZT thin film devices. In addition to acting as epitaxial templates for textured PZT growth, each type of electrode material has a unique surface with regard to roughness and conductivity or surface contact resistance. For deposition of PZT at high temperatures, sticking coefficients for the various PZT components can vary dramatically between electrode materials. As the sticking coefficients vary, the composition of the ferroelectric film varies. As the electrode surface begins to be coated by a layer of ferroelectric film, the sticking coefficients for the constituents change. This results in composition gradients at the ferroelectric/electrode interface that make it difficult to achieve the composition required for optimum electrical performance when using a single fixed set of sputtering conditions for the entire film thickness. During high temperature deposition and post-ferroelectric-deposition anneal, interdiffusion at the ferroelectric/electrode interface provides a second mechanism for the formation of composition gradients detrimental to achieving optimal

ferroelectric properties. Many researchers have opted to make specific adjustments in sputter deposition conditions or spin-on solution chemistry to compensate for the composition gradients at the PZT/electrode interface (5). Although this approach can improve on the desired sharp composition profile of the ferroelectric films at the electrode interface, it does not necessarily result in the optimum profile and ferroelectric properties.

To ensure a sharp ferroelectric/electrode interface profile, and prevent interdiffusion, the bottom electrode must exhibit a high density with a minimum of diffusion pathways (including pores and grain boundaries), and must remain stable without degradation of the density and topography. In addition to formation of a lead (Pb)-depleted ferroelectric/electrode interface, a low density electrode can in the extreme allow diffusion of Pb completely through the Pt and into the underlying SiO₂ layer. Reaction of the Pb and the SiO₂ causes formation of lead silicates that exhibit both crystalline and amorphous atomic structures, which can compromise the electronic properties of the substrate. In conjunction with lead silicate formation, pores are formed and the corresponding local loss of adhesion allows bubbles to form in the overlying thin film layers.

Because of the sensitivity of crystallographic fiber texture to composition, density, and surface roughness, texture is an extremely useful parameter for statistical process control (SPC) of Pt and PZT. In this study, we have used a powder diffractometer to obtain diffraction data for bottom-electrode TiO₂ and Pt. Quantitative analysis of the diffraction data was used to optimize the TiO₂ and Pt depositions to improve the density of the underlying layer in order to eliminate the Pt diffusion route, as well as to obtain a highly oriented fiber texture of the Pt, as evidenced by the 111 and 222 Pt rocking curves. The improved Pt orientation and optimization are being made to improve orientation, density, and relative alignment of grains for the PZT that will be deposited on top of it for PZT-MEMS applications.

The work presented in this report is based on and extends the studies by Fox et al. (2–4), who used X-ray diffraction (XRD) spectra of TiO₂ and Pt films to develop process control methods for SPC. For the present work, Ti films were sputtered under various conditions onto SiO₂/Si wafers in order to provide a growth template for subsequent Pt sputter depositions. Through studies of their dependence upon the Ti deposition power-time conditions and the Ti → TiO₂ conversion-anneal temperature-time conditions, orientation of the crystallites of both the TiO₂ and subsequent Pt thin films were optimized to obtain (1) maximum peak height and minimum full-width-at-half-maximum (FWHM) of 200 TiO₂, 111 Pt, and 222 Pt XRD peaks and (2) their respective rocking curves.

2. Experimental Procedures

2.1 Materials and Processing Description

Silicon (Si) substrates were obtained with 500 nm $\pm 5\%$ and $\pm 3.5\%$ thermal oxide from Addison and Silicon Quest International, respectively. Ti films were sputter-deposited on the as-received SiO₂ using the process module 1 (PM1) chamber of the Unaxis Clusterline 200. The Ti was then converted to TiO₂ with an oxygen anneal in a Bruce Technologies International 6-in. diameter tube furnace. The furnace was heated with 5 SLM flowing N₂ to the setpoint (650 °C–800 °C), the wafer boat was loaded and pushed into the tube hot zone over a period of 10 min. At the start of the wafer push step, the N₂ flow was turned off and the O₂ gas flow was ramped up to 10 SLM. At the end of the wafer push, the wafers were held in the hot zone for either 15 or 30 min. The boat was then pulled from the hot zone over a period of 10 min. When the wafers were fully retracted, the O₂ flow was turned off and the N₂ flow was resumed at 5 SLM. The wafers were removed from the boat loader after having been cooled for at least 10 min. After the oxidation anneal, Pt was sputter-deposited onto the TiO₂ using the Unaxis Clusterline 200 chamber PM4. All Pt depositions were completed with the same conditions of 500 W, 50 sccm Ar, 30.5 s and a substrate setpoint temperature of 500 °C. The plasma was struck after stabilizing Ar flow, and then power was ramped at 1 W/s. A Umicore sputtering target, 250 mm in diameter, nominally 12 mm thick and 99.99% pure, supplied by Unaxis, was used to make the depositions. Three test wafers were deposited prior to sample depositions using the same process in order to condition the chamber. Figure 1 shows the sequence of layers for the completed electrode layer.

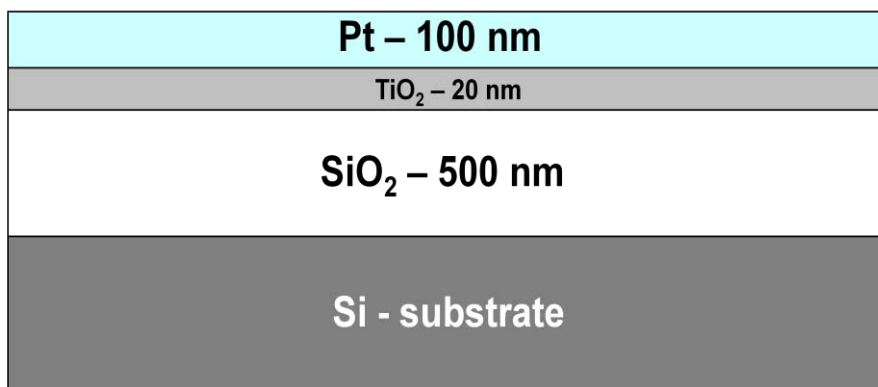


Figure 1. Sequence of layers composing the substrate and bottom electrode for PZT thin film growth.

Six experimental matrices of Ti and two matrices of TiO₂ processing conditions were completed. The Ti depositions were made by sputtering a 250-mm diameter, nominally 12-mm thick, and 99.99% pure Umicore Ti target supplied by Unaxis. Presputtering and sputtering conditions are displayed in tables 1–6. The objective of Matrix #1 was to determine the reproducibility and

uniformity of Ti films deposited under fixed conditions of 1,000 W/30 sccm Ar/19 s, but under varying pre-sputter times as shown in table 1. These deposition conditions were expected to result in a film thickness of 20 nm, but subsequent thickness measurements presented below indicate that the films were closer to 32 nm. In order to observe effects of target oxidation during chamber idling and any chamber heating effects, the first three wafers were deposited after the chamber was idle for at least 24 h. The fourth wafer in each split was coated using a sputter time of 95 s, which could be used as a process control monitor (PCM) for thickness and sheet resistance measurements. The PCM wafers were expected to have a thickness of 100 nm, but extrapolations from subsequent thickness measurements indicated that the actual PCM film thickness was 160 nm. After deposition of wafer 4, 45 depositions of 19 s each were run using dummy wafers in order to further study the effects of target pre-sputtering on subsequent 19 s and PCM (95 s) depositions. A final group of 90 pre-sputter dummy, 19-s deposition and PCM wafers completed the matrix. The substrates were held at a constant temperature during deposition by maintaining a heated chuck set-point temperature of 40 °C during deposition. Wafers were transferred from the load-lock into the alignment module, and then placed directly into the deposition chamber idling at 40 °C. After reaching a base pressure of 5×10^{-6} mbar, the Ar flow was turned on, the flow and chamber pressure were allowed to stabilize for 15 s, and the plasma was ignited and power ramped up at a rate of 1 W/s.

Table 1. Ti deposition matrix #1 with varying presputter time for evaluation of Ti deposition stability over time (targeted thicknesses = 20 nm and 100 nm and actual thicknesses = 32 nm and 160 nm for the 19 s and 95 s depositions, respectively). The fourth wafer in each split, coated using a sputter time of 95 s, could be used as a PCM for thickness and sheet resistance measurements.

	Wfr. No.	Pre-Sputter Time (s)	Dep. Time (s)	Sub. Temp. (°C)	Power (W)	Ar. Flow (sccm)
	1	0	19	40	1000	30
	2	19	19	40	1000	30
	3	38	19	40	1000	30
PCM - thickness	4	57	95	40	1000	30
	45xDummy	912	19	40	1000	30
	5	931	19	40	1000	30
	6	950	19	40	1000	30
	7	969	19	40	1000	30
PCM - thickness	8	988	95	40	1000	30
	90xDummy	2698	19	40	1000	30
	9	2717	19	40	1000	30
	10	2736	19	40	1000	30
	11	2755	19	40	1000	30
PCM - thickness	12	2774	95	40	1000	30

Tables 2 and 3 show the run order and deposition conditions for matrices that were used to characterize the effect of Ar flow rate (sputtering pressure is proportional to the Ar flow rate for these experiments since the Clusterline has a fixed throttle valve configuration) and cathode power on Ti deposition. Similar to Matrix #1, Matrices #2 and #3 use 19-s and 95-s depositions

to prepare films for characterization of the Ti film properties, deposition rate, and uniformity. A dummy wafer deposition was completed between each change in deposition conditions to allow stabilization of the chamber.

Table 2. Ti deposition matrix #2 with varying Ar flow for evaluation of change in Ti deposition rate and properties with Ar flow and corresponding deposition pressure.

	Wfr. No.	Dep. Time (s)	Sub. Temp. (°C)	Power (W)	Ar. Flow (sccm)
Dummy	21	95	40	1000	30
PCM	1	95	40	1000	30
	2	19	40	1000	30
	3	19	40	1000	30
	4	19	40	1000	30
Dummy	22	95	40	1000	10
PCM	5	95	40	1000	10
	6	19	40	1000	10
	7	19	40	1000	10
	8	19	40	1000	10
Dummy	23	95	40	1000	20
PCM	9	95	40	1000	20
	10	19	40	1000	20
	11	19	40	1000	20
	12	19	40	1000	20
Dummy	24	95	40	1000	50
PCM	13	95	40	1000	50
	14	19	40	1000	50
	15	19	40	1000	50
	16	19	40	1000	50
Dummy	25	95	40	1000	95
PCM	17	95	40	1000	95
	18	19	40	1000	95
	19	19	40	1000	95
	20	19	40	1000	95

Table 3. Ti deposition matrix #3 with varying applied cathode power for evaluation of change in Ti deposition rate and properties with deposition power.

	Wfr. No.	Pre-Sputter Time (s)	Dep. Time (s)	Sub. Temp. (°C)	Power (W)	Ar. Flow (sccm)
Dummy	-		900	40	1000	30
Dummy	1		95	40	1000	30
PCM	2		95	40	1000	30
	3		19	40	1000	30
	4		19	40	1000	30
	5		19	40	1000	30
Dummy	6		95	40	500	30
PCM	7		95	40	500	30
	8		19	40	500	30
	9		19	40	500	30
	10		19	40	500	30
Dummy	11		95	40	1500	30
PCM	12		95	40	1500	30
	13		19	40	1500	30
	14		19	40	1500	30
	15		19	40	1500	30
Dummy	16		95	40	2000	30
PCM	17		95	40	2000	30
	18		19	40	2000	30
	19		19	40	2000	30
	20		19	40	2000	30
Dummy	21		95	40	3000	30
PCM	22		95	40	3000	30
	23		19	40	3000	30
	24		19	40	3000	30
	25		19	40	3000	30

A series of wafers for use in an experiment for Ti oxidation anneals was generated according to table 4. This Matrix #4 also provided a second check on deposition reproducibility and uniformity for fixed deposition conditions. Prior to wafer deposition, a pre-sputter of 900 s was completed since the results from Matrix #1 indicated that coatings deposited before completing this pre-sputter did not exhibit consistent thickness and sheet resistance values.

Table 4. Ti deposition matrix #4 with fixed deposition conditions for evaluation of change in Ti deposition stability and preparation of wafers for oxidation anneal experiments.

	Wfr. No.	Pre-Sputter Time (s)	Dep. Time (s)	Sub. Temp. (°C)	Power (W)	Ar. Flow (sccm)
Dummy	Dummy		900	40	1000	30
PCM	1	900	95	40	1000	30
	2	995	19	40	1000	30
	3	1014	19	40	1000	30
	4	1033	19	40	1000	30
	5	1052	19	40	1000	30
	6	1071	19	40	1000	30
	7	1090	19	40	1000	30
	8	1109	19	40	1000	30
	9	1128	19	40	1000	30
	10	1147	19	40	1000	30
	11	1166	19	40	1000	30
	12	1185	19	40	1000	30
	13	1204	19	40	1000	30
	14	1223	19	40	1000	30
	15	1242	19	40	1000	30
	16	1261	19	40	1000	30
	17	1280	19	40	1000	30
	18	1299	19	40	1000	30
	19	1318	19	40	1000	30
	20	1337	19	40	1000	30
	21	1356	19	40	1000	30
	22	1375	19	40	1000	30
	23	1394	19	40	1000	30
	24	1413	19	40	1000	30
	25	1432	19	40	1000	30

Since some unexpected variability in Ti thickness and sheet resistance was observed in the results collected from some wafers in Matrices #1, 2, 3, and 4, Matrix #5, shown in table 5, was deposited using two substrate sources and the idle time between lot splits as variables. Wafers supplied by Addison and Silicon Quest International (SQI) had the same thermal oxide thickness of approximately 500 nm, as specified at the beginning of this section. The wafers were separated into three split lots and were processed on the dates listed in the table. The split for wafers 1–6 was processed after the Ti chamber was operated at 500 °C and then cooled to 42 °C. A pre-sputter of 900 s was completed before processing the wafers in the first split. After completing the first split, the chamber was allowed to cool and left idle for 80–90 hr, and then wafers 7–13 were processed. Finally, the chamber was used to process wafers at 500 °C, the chamber was allowed to cool and then wafers 14–21 were processed. The objective of this matrix was to determine whether the conditioning of the chamber—i.e., chamber heating, target heating, or residue on the target or shields—caused the variability observed in the Ti film properties.

Table 5. Ti deposition matrix #5 with fixed deposition conditions for evaluation of change in Ti deposition stability over time and the effect of substrate vender.

Date		Wfr. No.	Vendor	Pre-Sputter Time (s)	Dep. Time (s)	Sub. Temp. (°C)	Power (W)	Ar. Flow (sccm)
Friday, February 13, 2009	Dummy	Dummy	Addison		900	40	1000	30
		1	Addison	900	19	40	1000	30
		2	SQI	919	19	40	1000	30
		3	SQI	938	19	40	1000	30
		4	Addison	957	19	40	1000	30
		5	SQI	976	19	40	1000	30
		6	Addison	995	19	40	1000	30
Tuesday, February 17, 2009	Dummy	7	Addison		900	40	1000	30
		8	SQI	900	19	40	1000	30
		9	Addison	919	19	40	1000	30
		10	Addison	938	19	40	1000	30
		11	SQI	957	19	40	1000	30
		12	Addison	976	19	40	1000	30
		13	SQI	995	19	40	1000	30
Wednesday, February 18, 2009	Dummy	14	Addison		900	40	1000	30
		15	Addison	900	19	40	1000	30
		16	SQI	919	19	40	1000	30
		17	Addison	938	19	40	1000	30
		18	SQI	957	19	40	1000	30
		19	Addison	976	19	40	1000	30
		20	SQI	995	19	40	1000	30

The final experiment, Matrix #6 shown in table 6, varied the Ti film thickness by changing the deposition time between 6 s and 38 s. Two different cathode powers were used to obtain two sets of wafers with Ti thicknesses between 10–45 nm.

Table 6. Ti deposition matrix #6 with varying deposition time and power to obtain Ti thickness between 10 nm and 45 nm for evaluation of Ti, TiO₂, and Pt properties.

		Cumulative Sputter Time (s)	Dep. Time (s)	Sub. Temp. (°C)	Power (W)	Ar. Flow (sccm)
Wfr. No.	Dummy					
PCM	Dummy		900	40	1000	30
	1	900	95	40	1000	30
	2	995	19	40	1000	30
	3	1014	19	40	1000	30
	4	1033	19	40	1000	30
	5	1052	25	40	1000	30
	6	1077	25	40	1000	30
	7	1102	25	40	1000	30
	8	1127	12	40	1000	30
	9	1139	12	40	1000	30
	10	1151	12	40	1000	30
	11	1163	9	40	1000	30
	12	1172	9	40	1000	30
	13	1181	9	40	1000	30
	14	1190	6	40	1000	30
	15	1196	6	40	1000	30
	16	1202	6	40	1000	30
Dummy	Dummy	1208	190	40	500	30
	17	1398	38	40	500	30
	18	1436	38	40	500	30
	19	1474	38	40	500	30
	20	1512	24	40	500	30
	21	1536	24	40	500	30
	22	1560	24	40	500	30
	23	1584	18	40	500	30
	24	1602	18	40	500	30
	25	1620	18	40	500	30

An oxygen anneal study where the temperature was varied over the range 650–800 °C, and anneal time was either fixed at 15 min or 30 min was applied to the Ti films deposited in Matrix #4. The wafers were oxidized in groups of three using the Bruce Technologies tube furnace with 10 SLM flowing O₂, as described previously. Two additional Ti oxidation studies were completed on Matrices #5 and #6 using the fixed anneal conditions of 750 °C/15 min/10 SLM and 700 °C/15 min/10 SLM, respectively.

2.2 Thin Film Sheet Resistance Characterization Procedures

The sheet resistances, R_s, of Ti and Pt films were measured on a Prometrics Versaprobe VP10 and a Four Dimensions Model 280 Automatic Four-Point Probe Meter, respectively. A wafer map showing the positions for the Ti and Pt measurements is shown in figures 2 and 3, respectively. Because the sheet resistance measurement is fast and sensitive to film thickness,

structure, and impurities, it will be the primary parametric measurement for SPC of Ti and Pt depositions.

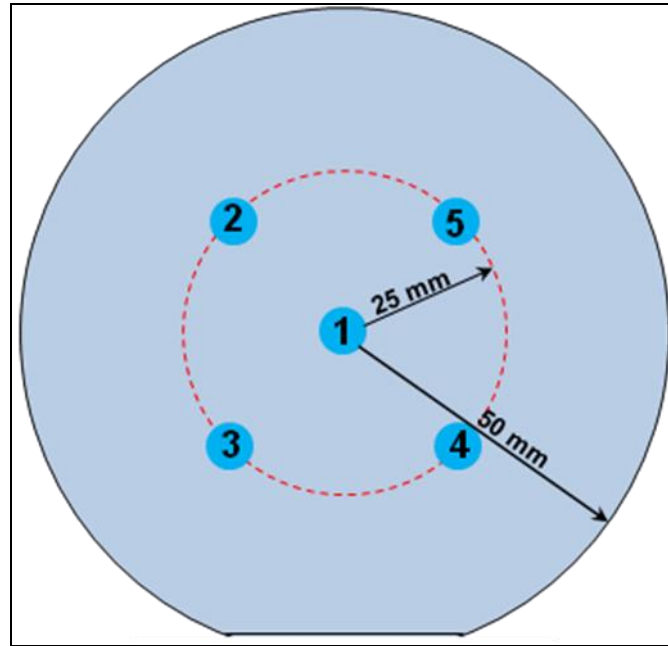


Figure 2. Positions for Ti thin film sheet resistance measurements with 4-point probe.

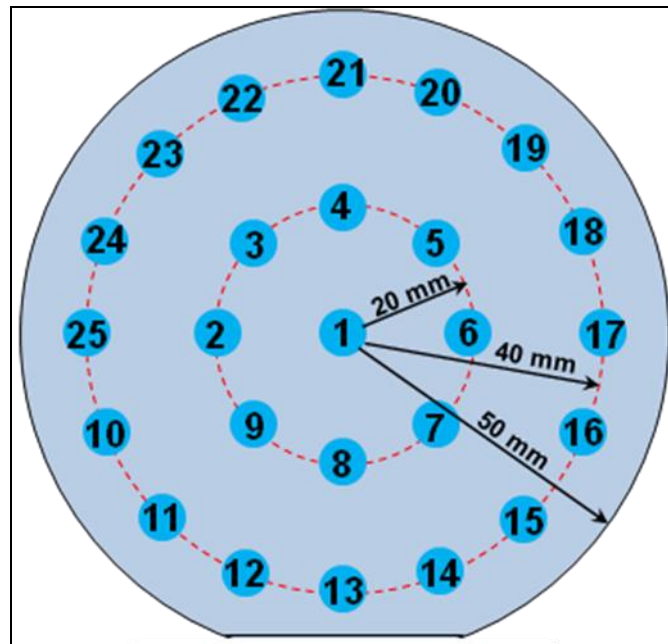


Figure 3. Positions for Pt thin film sheet resistance measurements with 4-point probe.

2.3 Thin Film Thickness and Refractive Index Characterization Procedures

A JA Woollam ellipsometer, model M-2000F, was used for measuring the thickness and refractive index of the as-received SiO_2 coatings and the annealed TiO_2 films. The SiO_2 and TiO_2 films were treated as dielectric films on an infinitely thick silicon substrate, and the silicon substrate was modeled using reference data from Herzinger et al. (6). The thicknesses and refractive indices for the TiO_2 and SiO_2 films were extracted by fitting a Cauchy model to the experimental data collected at a fixed angle of 65° and over a wavelength range of 240–1000 nm. Figure 4 shows a wafer map with the ellipsometer measurement positions. The set-up parameters for the SiO_2 and TiO_2 measurements are given in table 7. Using ellipsometry, the TiO_2 thickness was determined to be 31.0–32.5 nm for the oxidized Ti films deposited in Matrix #4, and 20.5–43.0 nm for oxidized films deposited in Matrix #6. The TiO_2 refractive index at a wavelength of 1000 nm was 2.63–2.67 for Matrix #4 and 2.53–2.68 for Matrix #6. In the latter case, the index increased with larger film thickness, and the index for a smaller subset of three samples in Matrix #6 (1,000 W, 19 s) was nominally the same as for TiO_2 samples in Matrix #4, all these samples being similar in thickness (31.0–33.0 nm).

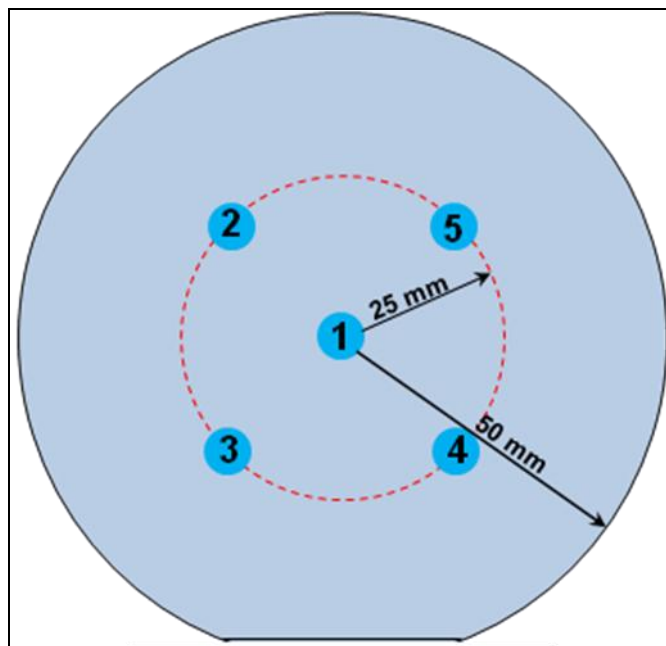


Figure 4. Positions for ellipsometry measurements of SiO_2 and TiO_2 coatings.

Table 7. SiO_2 and TiO_2 ellipsometry measurements.

Thin Film	Trial Thickness	Optical Parameters
SiO_2	500 nm	See reference 7
TiO_2	30 nm	Cauchy layer: $A_n \sim 2.5$, $B_n \sim 0.05$

2.4 Crystallinity Characterization Procedures

The characterization of Pt and PZT thin film crystallinity and crystalline texture by XRD has been well-developed, but the procedures vary considerably between research institutes. One of the least complex, but most accurate and quickest procedures is to employ a powder diffractometer with Bragg-Brentano X-ray optics. The U.S. Army Research Laboratory (ARL) has three XRD tools that are easily accessible—a Bruker Quarter Circle Chi Platform System with Area Detector, Panalytical MRD PRO, and Rigaku Ultima III.

Cursory evaluations of all three XRD systems were completed to determine the ease of application for detailed and SPC characterization of Pt and PZT films. Since the Bruker employs an area detector, new crystalline phase and texture quantification procedures would need to be developed; therefore, the Bruker was eliminated from the list of XRD tools that could quickly be used for film characterization. The Panalytical has a standard scintillation point detector, but it is configured with a double-bounce monochromater for high precision work. The double-bounce monochromater significantly reduces the X-ray intensity incident upon the sample and, thus, reduces signal strength for TiO₂ and PZT to the point that critical diffraction peaks cannot be detected. By reconfiguring the Panalytical, removing the double-bounce monochromater, and moving the X-ray source inward to a symmetric position about the diffractometer axis, the low intensity problem could be solved, but this would be at the expense of having to realign the tool every time the configuration is changed. Reconfiguration of the Panalytical is a possible but impractical solution because it would make its use extremely inconvenient for both sets of users, those requiring the high resolution and those requiring the lower resolution Bragg-Brantano configuration. The Panalytical does provide several advantages over the Rigaku, including a motorized wafer holder and chi angle measurements, but the disruption to other groups at ARL cannot justify reconfiguring the Panalytical for regular measurements of PZT, Pt, and TiO₂.

Fortunately, the Rigaku diffractometer meets the requirements for configuration and accessibility for characterization and SPC of Pt, PZT, and related materials development. The Rigaku has two standard configurations, Bragg-Brentano and parallel beam optics, that easily interchange without diffractometer realignment. Through regular monitoring of alignment with a standard, the Rigaku can provide highly reproducible quantitative results for θ -2 θ and θ - θ (rocking-curve) measurements of thin film PZT, Pt, TiO₂, and Ti. There are a few disadvantages to using the Rigaku—namely, it has a fixed spring-clip sample holder that can scratch the surface of the wafer and does not allow measurements of the middle 3–4 cm diameter area of a 4 in wafer. All data presented in this report was collected using the Rigaku Ultima III and with the following procedures.

2.5 Rigaku Diffractometer Setup and Calibration Check

A detailed description of the Rigaku diffractometer set-up is included in the attached appendix A. The Rigaku is equipped with a copper (Cu) X-ray tube and a monochromator. The monochromator is mounted on the detector arm and allows CuK α_1 and CuK α_2 characteristic

radiation to pass to the detector. Only single-site measurements are reported due to the limitations of the spring-clip sample holder. Wafers were inserted into the spring-clip sample holder with the wafer flat facing the back of the diffractometer and with the wafer edge in contact with the vertical surface of the holder. Since standard 4-in diameter wafers are too thin to be held securely, a 1.5-mm thick alumina plate was placed in contact with the backside of the wafer and inserted into the spring-clip along with the wafer. Because this diffractometer is used by other groups to measure powder samples, it is recommended that the spring-clips and holder be wiped with isopropanol before starting measurements.

At the start of each measurement session, a calibration check of the diffractometer should be completed. A calibration check based on an alumina standard has been established since a randomly oriented alumina plate with a thickness that is similar to the wafer samples is readily available at a low cost (Coors Ceramic, single-side polished 96% alumina wafer, 100 mm diameter, 500 μm thickness). Comparison of these alumina plates with National Institute of Standards and Technology (NIST)-traceable alumina standards, and International Centre for Diffraction Data (ICDD) card number 10-0173, exhibits intensities and peak positions within the measurement errors of the Rigaku Ultima III diffractometer. The measurement conditions for the alumina standard (listed at the bottom of table 8) were chosen in order to obtain a calibration check within a short time period, while maintaining sufficient resolution and signal-to-noise levels to ensure accuracy.

Table 8. Alumina $\text{CuK}\alpha_1$ peak position, intensity and measurement ranges used for diffractometer calibration check.

Peak Index	ICDD 2θ (°)	ICDD Relative Int. (%)	2θ Meas. Range (°)	Avg. Meas. 2θ (°)	Avg. Intensity (cps)
012	25.5835	75	24.0/27.0	25.57 ± 0.02	$2125 \pm 5\%$
116	57.5177	80	56.0/59.0	57.49 ± 0.01	$5433 \pm 5\%$
226	95.2597	14	94.0/97.0	95.25 ± 0.01	$493 \pm 5\%$
Scan Type = 0 - 2θ (continuous)					
Scan Rate = 1.0 deg/min					
Step Size = 0.01 deg					

2.6 Measurement Procedure for Ti, TiO_2 , Pt and PZT Thin Films

XRD measurements for the Ti, TiO_2 , Pt, and PZT films have two objectives. The first objective is to provide a means to quantitatively characterize the crystalline phases and texture formed by each process, and to use the information for process modification by creating a process/crystallinity map. The second objective is to provide a quantitative method to monitor the crystalline phase and texture produced by an established process—i.e., to provide an SPC method. Whenever possible, it is preferred that both objectives are attained within the same measurement, but this is not always possible since SPC requires high speed measurements to achieve high throughput, and characterization requires high resolution for high accuracy. It can be concluded from the two desired objectives that there is always a trade-off between high-speed

and high-precision/high-accuracy conditions when trying to combine SPC and characterization into a single measurement. The first step in attaining SPC and characterization objectives within a single measurement is to ensure XRD calibration and measurement reproducibility with a standard, as described previously. The standard measurement should be completed with conditions similar to the conditions used for the SPC and characterization samples. Once the calibration procedure is established, the second step is to ensure that the diffractometer is always operated within its linear detection range. For the Ultima III, it has been confirmed that the detector remains linear up to 10^5 cps. In order to avoid errors that could be introduced by numerically correcting spectra for nonlinearities, the intensities of all spectra for quantitative analysis will be maintained within the linear range by using attenuating foils or slits within the beam path.

After ensuring that the diffractometer always provides consistent, linear measurements, it is necessary to determine the specific quantitative measurement that can be used for both film characterization and SPC. A variety of initial measurements were used for characterizing the Ti, TiO_2 , Pt, and PZT films. A general θ - 2θ continuous scan from 10° to 90° at a rate of $2^\circ/\text{min}$ and a step size of 0.01° was first completed on the film samples. The general scan provides the data required for phase identification and allows peaks to be identified for additional analysis. θ - 2θ continuous scans of individual peaks for quantitative measurements were typically completed with a scan rate of $0.1^\circ/\text{min}$ and a step size of 0.01° . Additional θ - θ (rocking curve) measurements with a scan rate of $0.5^\circ/\text{min}$ and a step size of 0.01° were completed in order to characterize the tilt distributions of specific crystallographic planes via the rocking curve FWHM.

As already described, the detected diffraction peaks included $\text{CuK}\alpha_1$ and $\text{CuK}\alpha_2$ characteristic radiation that could not be fully resolved for low angle measurements; therefore, a single peak Pearson VII algorithm was used to fit the experimental peak and obtain quantitative values of peak characteristics. Gaussian and Lorentzian peak fits were also investigated, but it was determined that the Pearson VII fit provided the highest accuracy and precision. The TiO_2 films were evaluated by using samples selected from each processing condition and by comparing Pearson VII FWHM, 2θ peak position, and peak-height (maximum) for 200 and 400 diffractions. In addition, rocking curves of the 200 diffraction peak were collected and evaluated by comparing RC-FWHM, θ peak position, and RC-peak-height from Pearson VII fits. The rocking curves were only measured on selected samples that were representative of the different processing conditions used in the Ti deposition in Matrices #2–6, Ti-oxidation in Matrix #4, and Ti-anneal in Matrix #6. It should be noted that samples in Matrix #6, with TiO_2 thicknesses of 16.5 nm or less, did not exhibit sufficient diffracted intensity to detect the 200 peak. Similar XRD data were obtained from 2θ scans and rocking curve measurements of the Pt 111 and Pt 222 peaks. In contrast with the TiO_2 diffraction data, the Pt-111 diffraction peaks were of such high intensity that there was concern about saturating the X-ray detector. Because the higher-angle Pt 222 peak provided a lower intensity than the Pt 111 peak, the Pt 222 peak was used to

assure that all quantitative measurements were collected in the linear response range of the diffractometer detector.

3. Results and Discussion

3.1 Ti Deposition and Effect of Sputtering Conditions

Sheet resistance measurements of Ti films deposited in Matrix #1 are plotted in figures 5 and 6 as a function of wafer number (in the order of deposition) and cumulative presputter time prior to deposition. Both plots indicate the occurrence of three regions that can be described as (1) target surface preclean that occurs just after the plasma strike; (2) target/chamber heating and preconditioning that occurs within the first 900 s of presputter, and shows a reduced sheet resistance; and (3) steady-state deposition that exhibits an upper limit, $UL = 64.7 \Omega/\text{sq}$, mean, $X = 62.7 \Omega/\text{sq}$, and lower limit, $LL = 60.8 \Omega/\text{sq}$. The UL and LL are three standard deviations (3σ) from the mean determined from all measurement sights shown in figure 2; therefore, the limits describe wafer-to-wafer variability and cross-wafer non-uniformity that can be used for SPC. Because the sheet resistance of deposited Ti remained stable after deposition of wafer #3, a 900-s pre-sputter was chosen as the preconditioning time for future Ti deposition lots. It may be possible to reduce this pre-conditioning time, but additional experiments are required to investigate the shorter pre-sputter times.

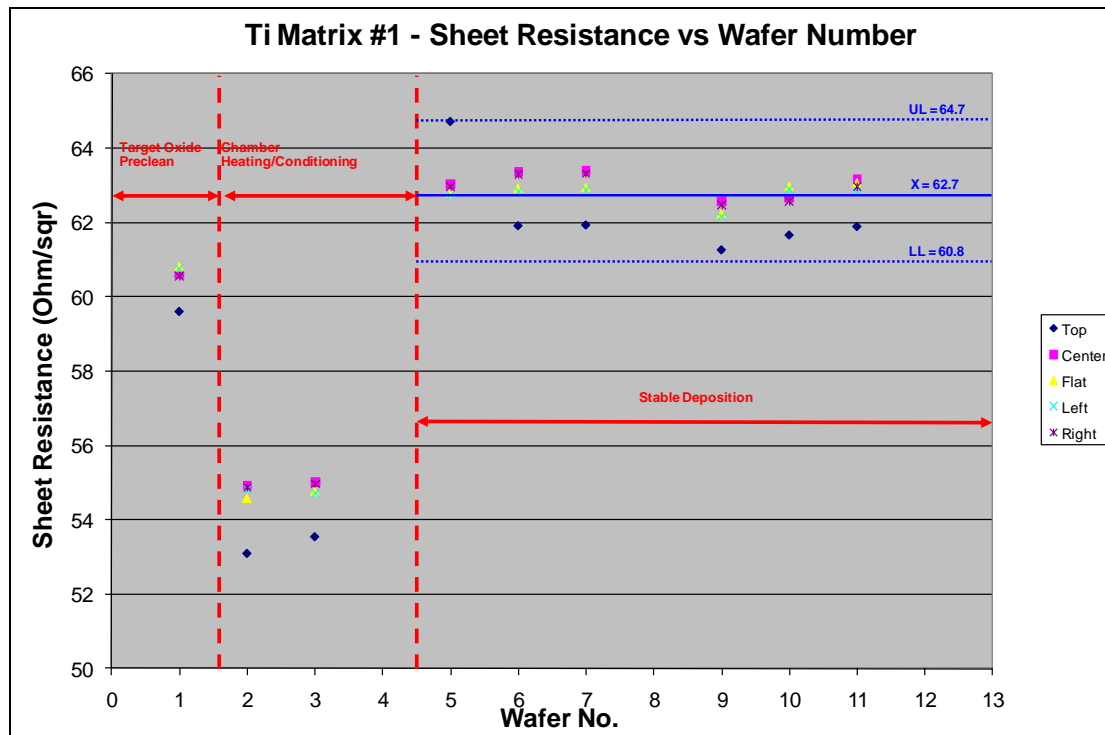


Figure 5. Five-site sheet resistance as a function of wafer number and deposition order for Ti deposited on Matrix #1 wafers.

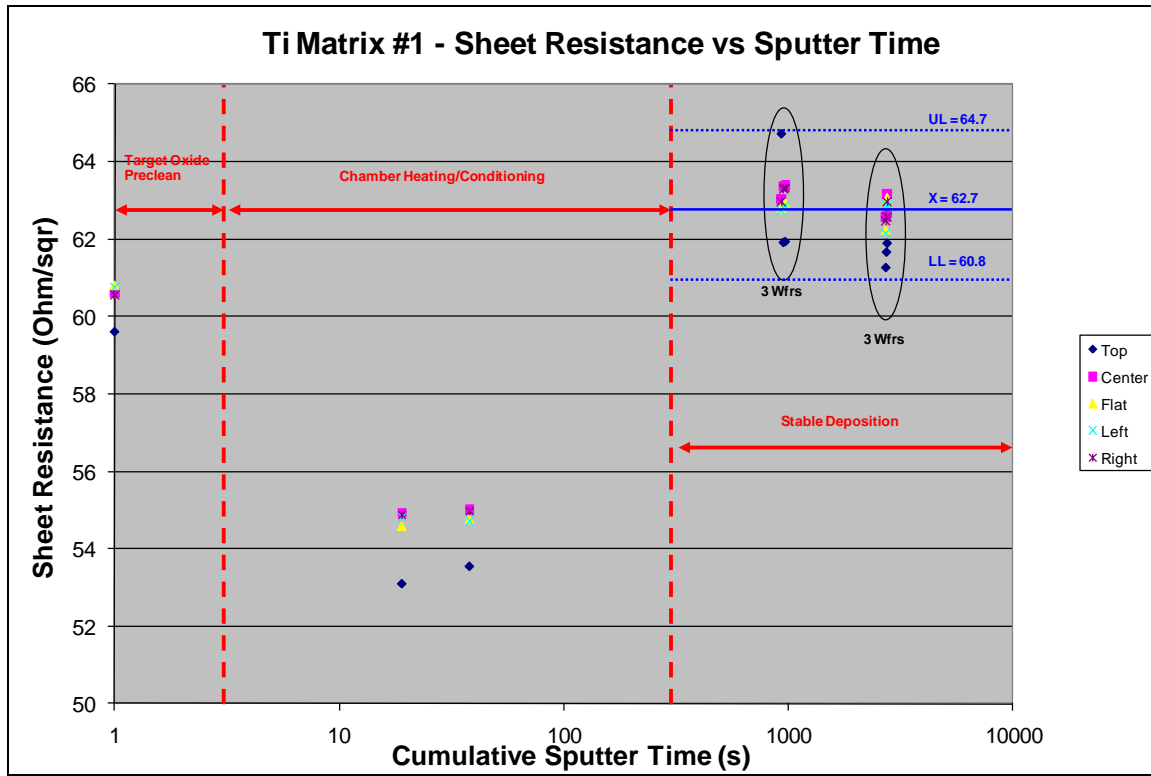


Figure 6. Five-site sheet resistance as a function of cumulative sputter time for Ti deposited on Matrix #1 wafers.

One plausible explanation for the variation in sheet resistance between the three regions in figure 2 is as follows. In region (i), oxidation of the target surface can cause a reduction in the sputtering rate, reducing the thickness of the deposited Ti film within the 19-s time period. In addition, oxygen and other impurities released by the target and chamber walls can be gettered by the film. Both these effects will reduce the sheet resistance of the film in region (i). Once any target surface oxide is removed, region (ii) is entered and the deposition rate and resulting film thickness increases, thus decreasing the film sheet resistance. Region (iii), with an increased sheet resistance, could result from target and chamber heating by the plasma. The increased temperature can cause increased outgassing of impurities, such as oxygen, from the chamber and also increases the probability of incorporation within the depositing film. Target and chamber heating can also reduce the deposition rate. Again, increased impurity levels and reduced film thickness will increase the sheet resistance in region (iii). The remaining Ti deposition results will be presented with regard to this explanation.

Wafers coated with Ti for a deposition time of 95 s (160 nm thickness) exhibited constant sheet resistance both before and after the 900-s chamber pre-conditioning period. This suggests that the thick PCMs are not sensitive to the variability observed in the 32-nm films deposited during chamber pre-conditioning. For this reason, measurements on the thin films to be used directly for

oxidation experiments were used for process monitoring instead of measurements from thick films. A summary of results for the 32-nm and 160-nm films is given in table 9.

Table 9. Summary of sheet resistance measurements and 3σ limits determined from Matrix #1 for SPC of Ti films deposited at 1,000 W/30 sccm Ar.

Thickness (nm)	Deposition Time (s)	Mean R_s (Ω/sq)	σ (Ω/sq)	σ (%)	UL (Ω/sq)	LL (Ω/sq)
32	19	62.75	0.65	1.0	64.69	60.81
160	95	8.23	0.47	5.7	9.64	6.81

After establishing the Ti pre-sputter procedure and confirming that steady-state deposition can be achieved within 3σ LL and UL limits of $\pm 3.1\%$ for 32 nm films, the sensitivity of deposition rate, uniformity, and repeatability to Ar flow rate were determined by running Matrix #2. Figure 7 shows a plot of the sheet resistance for each of the deposition conditions, with a fixed cathode power of 1,000 W, deposition time of 19 s, and variable Ar flow from 10 to 95 sccm, which induces a corresponding increase in chamber pressure. As is typical with an increase in Ar flow/pressure for the operating range of the magnetron sputtering chamber, the sheet resistance is observed to increase with flow at a rate of $0.16 \Omega/\text{sq}$ due to reduction in Ti deposition rate. Linear regression fits of the data are used to provide quantitative approximations to the dependence of R_s on Ar flow, but it should be noted that the linear approximation is only valid over the small Ar flow range shown in figure 7. The R_s magnitude changes in a sublinear fashion at both low and high Ar flow rates. Increased pressure causes a decrease in deposition rate and film thickness. It is also observed that the cross-wafer non-uniformity increases with increasing pressure. Both effects are caused by an increase in scattering events between sputtered species and the chamber gas, during the flight between the target and the substrate. It should be noted that the R_s values plotted for the 30 sccm condition do not fall within the UL and LL determined from Matrix #1. It appears as though all the films within Matrix #2 have a reduced sheet resistance (probable higher thickness) than those deposited in Matrix #1. This shift is disconcerting since it suggests that there is an unknown variable affecting the reproducibility of the thin Ti films. It can also be noted that the 30 sccm values do not fall exactly on the linear regression fits of the data. The slight shift upward from the linear dependence may be due to the fact that a 500 °C Ti deposition was run prior to Matrix #2, and the chamber may not have cooled sufficiently before running the 30 sccm wafers, which were first in the lot. This explanation would be consistent with the chamber heating effect we have described.

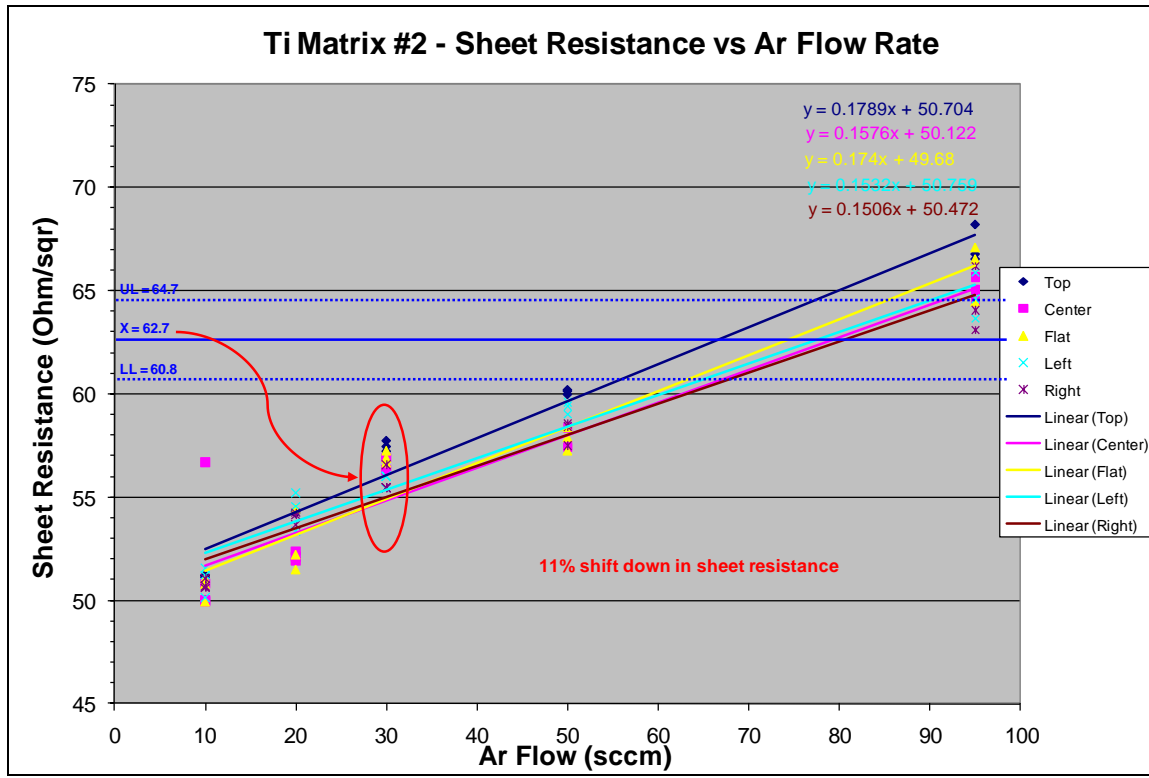


Figure 7. Five-site sheet resistance as a function of Ar flow rate (pressure) for Ti deposited on Matrix #2 wafers. The 0.16 Ohm/sq/sccm increase in sheet resistance with flow rate is due to a reduction in Ti deposition rate.

A clue about the cause for the suspected general downward shift in the sheet resistance observed for Matrix #2 can be determined from the magnitude of the shift. Because the magnitude of the reduced R_s is 11%, it is unlikely that errors in Ar flow/pressure can be the root cause for the R_s shift. According to figure 7, an error in Ar flow of approximately 50 sccm would be required to cause an 11% shift in R_s . Since such an error would account for 50% of the Ar flow controller range, such an error is unlikely under normal flow controller operation. Only a malfunctioning flow controller or pressure fluctuations due to improper isolation of the gas source line could cause such a large gas flow-induced variation in sheet resistance. Similar to the R_s shifts observed for the thin Ti films, R_s shifts are also observed with the thicker (approximately 160 nm) PCM films, indicating that the shifts are due to changes in the film thicknesses rather than sheet resistance measurement errors. Continued discussion of the shifts in R_s for Matrix #2 will be presented in more detail.

The average R_s for Matrix #4, in which wafers were coated with Ti under the same fixed conditions 1,000 W/30 sccm Ar/19 s used for Matrix #1, is shown in figure 8 as a function of cathode pre-sputter time. Note that all but two of the wafers exhibited R_s values within the expected LL and UL listed in table 9. A mechanical positioning failure of the wafer deposited at a pre-sputter time of 1261 s may be the cause of its reduced R_s , but there is no obvious explanation for the reduced R_s for the last wafer coating at 1432 s. Figure 9, a composite SPC

chart of Matrix 1, 2, and 4, shows that except for these two wafers, all of the wafers in Matrix #4 (wafer numbers 38 to 62) fall within the same UL and LL established from Matrix #1 (wafer numbers 1 to 12) and consistent with deposition under the same fixed conditions. The combined results from Matrix #1, 2, and 4 suggest that the intermittent variability in the Ti sheet resistance could originate from an error in wafer positioning, deposition timing, power control, or chamber history. Before continuing the discussion on the intermittent R_s variability, results from the remaining experimental matrices will be presented.

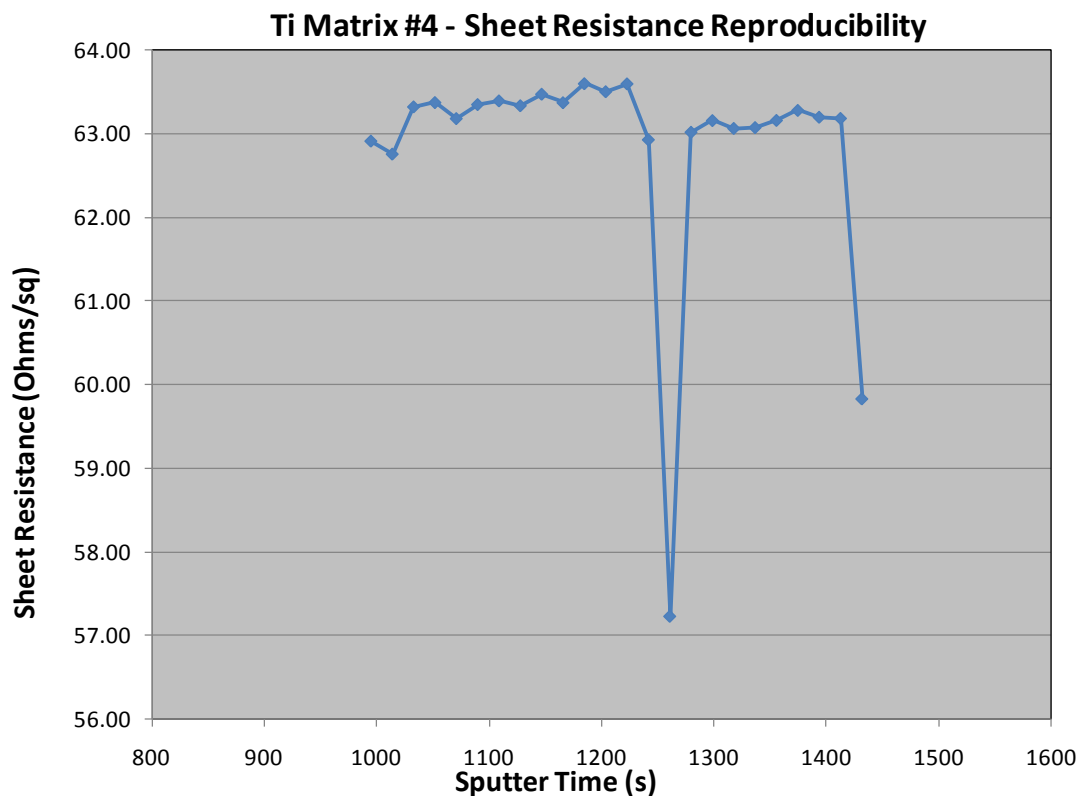


Figure 8. Average five-site sheet resistance measurement for 24 wafers deposited at the same fixed conditions of 1,000 W/30 sccm Ar/19 s from Ti Matrix #4. The decrease in sheet resistance for wafer #16 (with sputter time of 1261 s) results from a wafer positioning problem and possibly some other unidentified process variable.

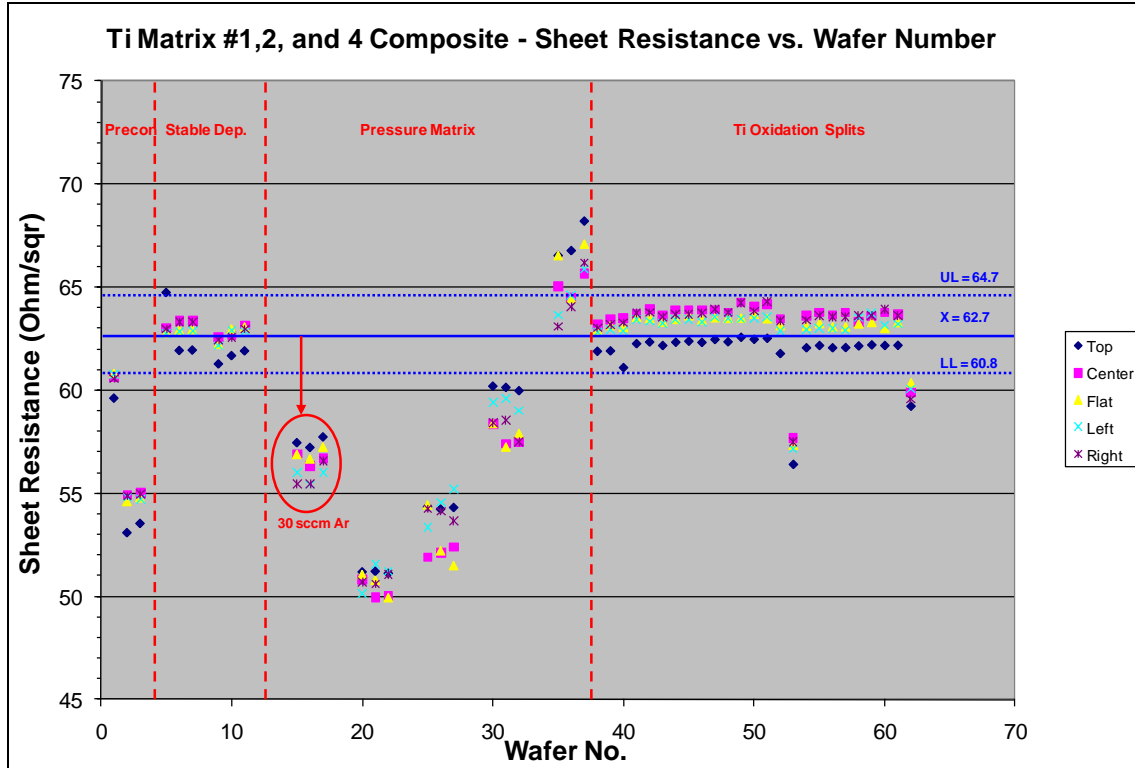


Figure 9. Composite plot of sheet resistance values for wafers deposited in Ti Matrix #1, 2, and 4. Wafers deposited at the same fixed conditions of 1,000 W/30 sccm Ar/19 s should exhibit sheet resistance values within the upper and lower limit lines.

Results from experimental Matrix #3 investigating the cathode power dependence of the R_s are plotted in figure 10. As expected, increasing power increases deposition rate and the resulting film thickness, thus reducing film sheet resistance. By plotting $1/R_s$ as a function of the power, a linear dependence is observed, and the slope is proportional to the deposition time, as shown in figure 11. Since the R_s is inversely proportional to the film thickness, these results confirm that the deposition rate and film thickness is proportional to cathode power for fixed Ar flow rate and deposition time. Extrapolation of the linear regression fits to zero $1/R_s$ in figure 11 results in a non-zero power value due to two factors. First, there is a critical power required to initiate sputtering from the target, and second, minimum film thickness is required for film continuity and measurement by four-point probe. The difference between the critical onset power levels, 391 W and 218 W for the 19 s and 95 s depositions times, is not understood and requires additional experimental work to develop an explanation. It should be noted that the results from Matrix #3 are also shifted downward (similar to Matrix #2) with respect to the UL and LL limits defined in table 9. The shift is expected to affect the R_s magnitudes at each power but not the change in R_s with power—i.e., the slope of the linear dependence.

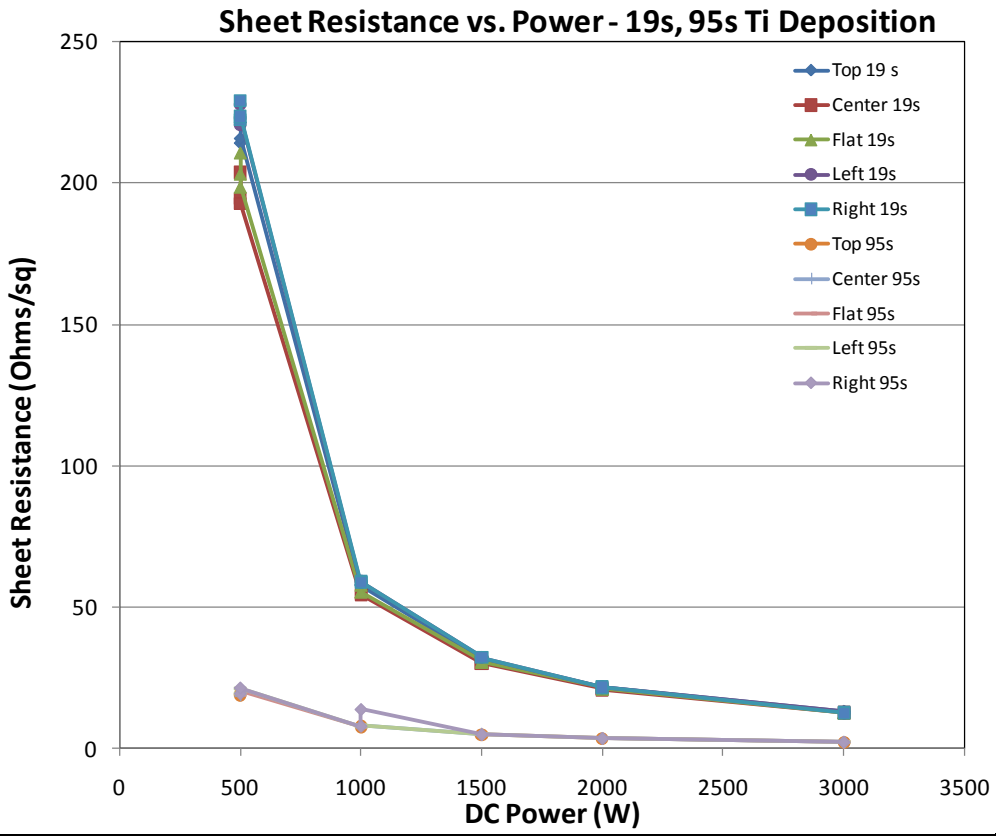


Figure 10. Ti Matrix #3 film R_s dependence on cathode power for fixed deposition times of 19 s and 95 s and a fixed Ar flow rate of 30 sccm.

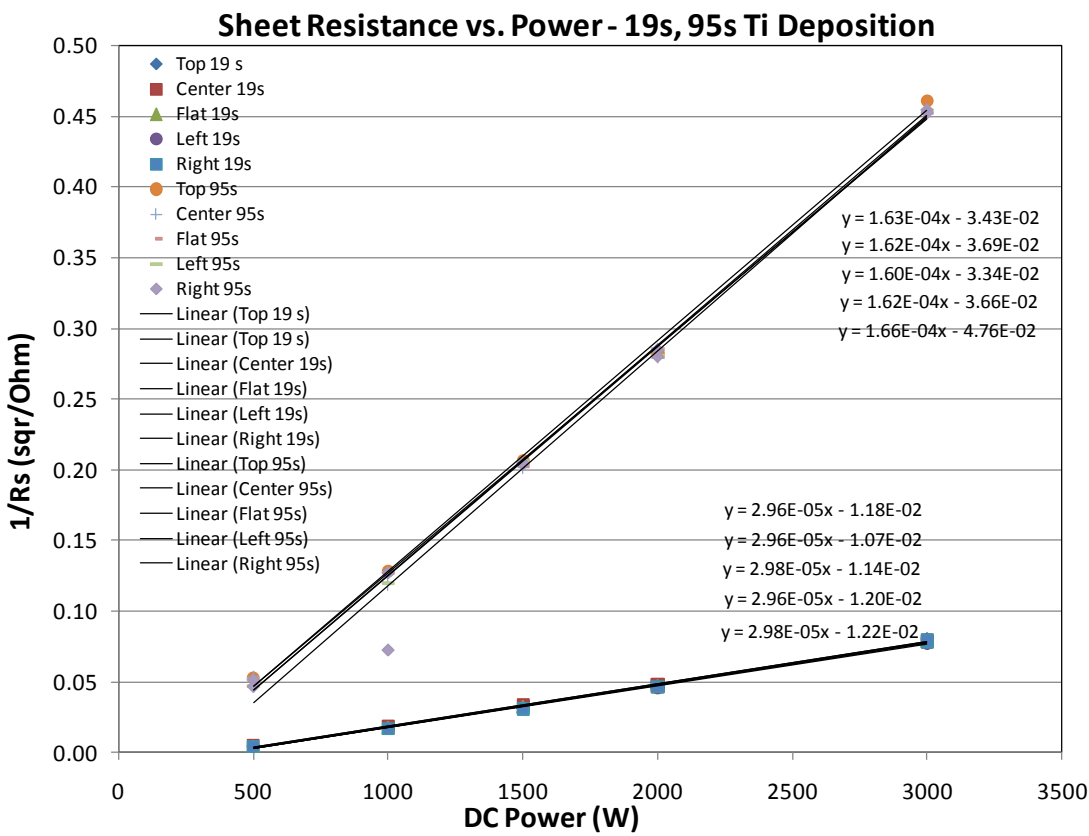


Figure 11. Ti Matrix #3 film $1/R_s$ dependence on cathode power for fixed deposition times of 19 s and 95 s and a fixed Ar flow rate of 30 sccm. Linear regression fit equations provide for calculation of R_s for SPC adjustments.

In order to confirm Ti deposition rate consistency with varying deposition time, a series of Ti films were deposited at various deposition times 500 W and 1,000 W cathode powers and a fixed Ar flow rate of 30 sccm. The R_s was measured on the as-deposited Ti films. The film thickness was measured by ellipsometry after converting the Ti to TiO_2 by an oxidation anneal at 700 °C/15 min/10 SLM O_2 . Since the density of Ti metal (4.508 g/cm^3) is within 6% of that for rutile (4.25 g/cm^3), it is more accurate to use the measured TiO_2 thickness than to determine Ti thicknesses from profilometry measurements. Results from Ti deposition Matrix #6 are summarized in figures 12 and 13. A linear regression fit forced through the origin (0,0) of the TiO_2 thickness vs deposition-time plot (figure 13) confirms the stability of the deposition rate at both 500 and 1,000 W. The linear $1/R_s$ dependence on Ti film thickness is also confirmed as shown in figure 14. Linear regression fits nearly overlap for the films deposited at 500 and 1,000 W, indicating that differences in deposition conditions have no significant effect on R_s . The change in $1/R_s$ with thickness is constant at an average value of $7.78 \times 10^{-4} \text{ sq}/\Omega \cdot \text{nm}$. The changes in R_s and $1/R_s$ with deposition parameters are summarized in table 10.

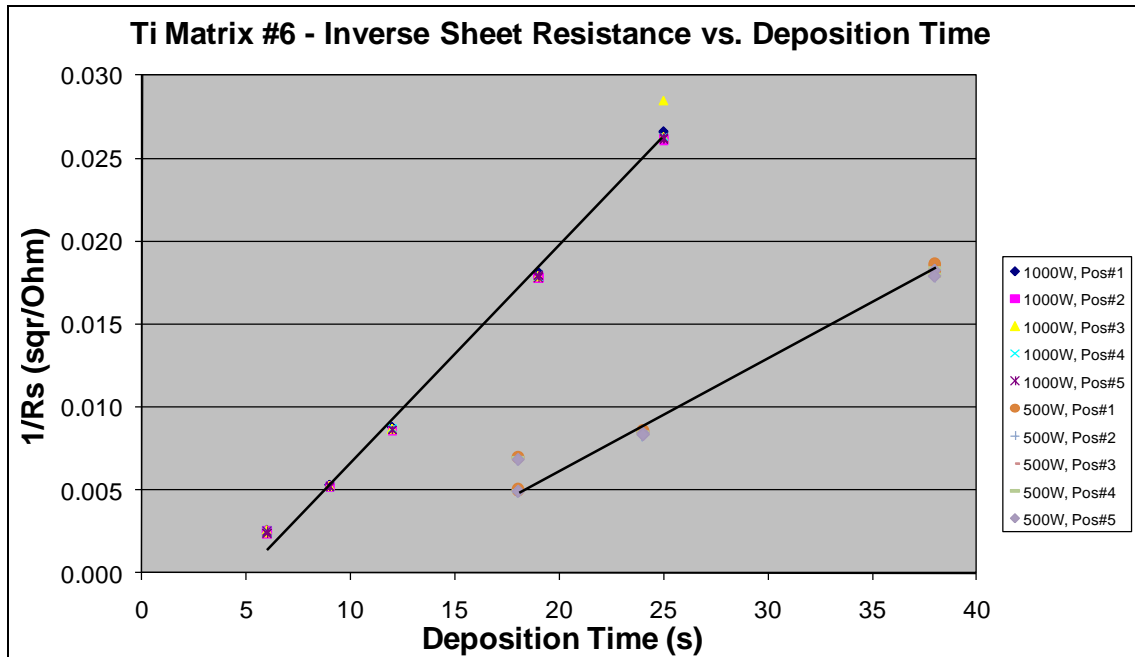


Figure 12. Ti film linear $1/R_s$ dependence on deposition time for fixed cathode powers of 500 W and 1,000 W and a fixed Ar flow rate of 30 sccm. Data is taken from Ti film Matrix #6.

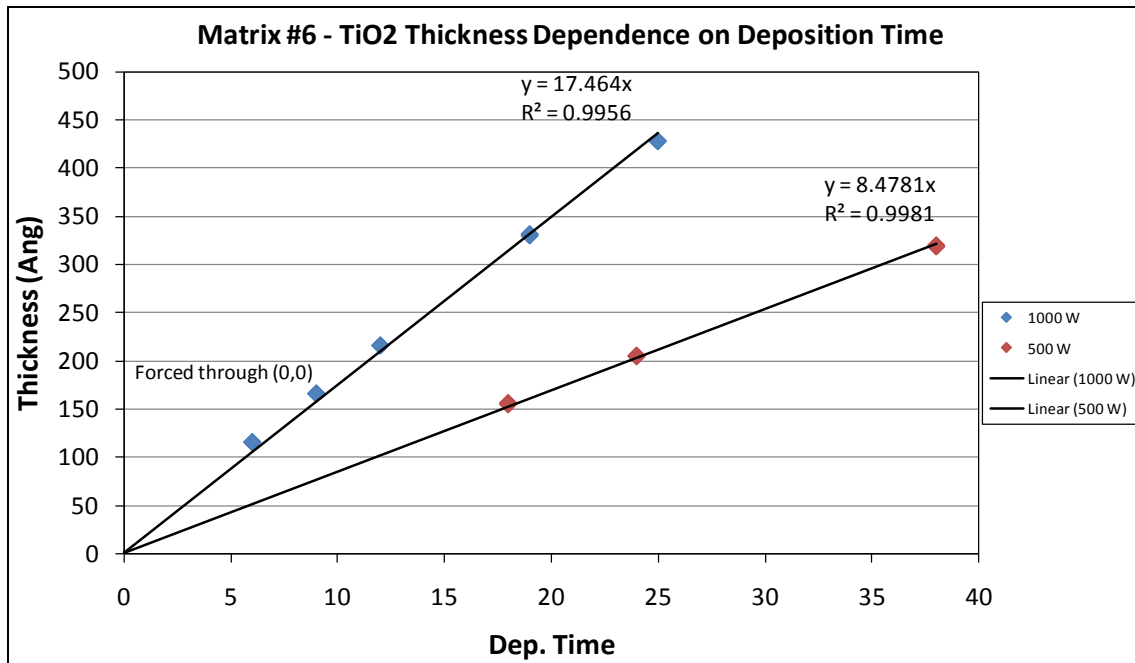


Figure 13. TiO₂ thickness dependence on deposition time at 500 W/30 sccm Ar and 1,000 W/30 sccm Ar with 700 °C/15 min post anneal. Data from three wafers are plotted for each deposition time.

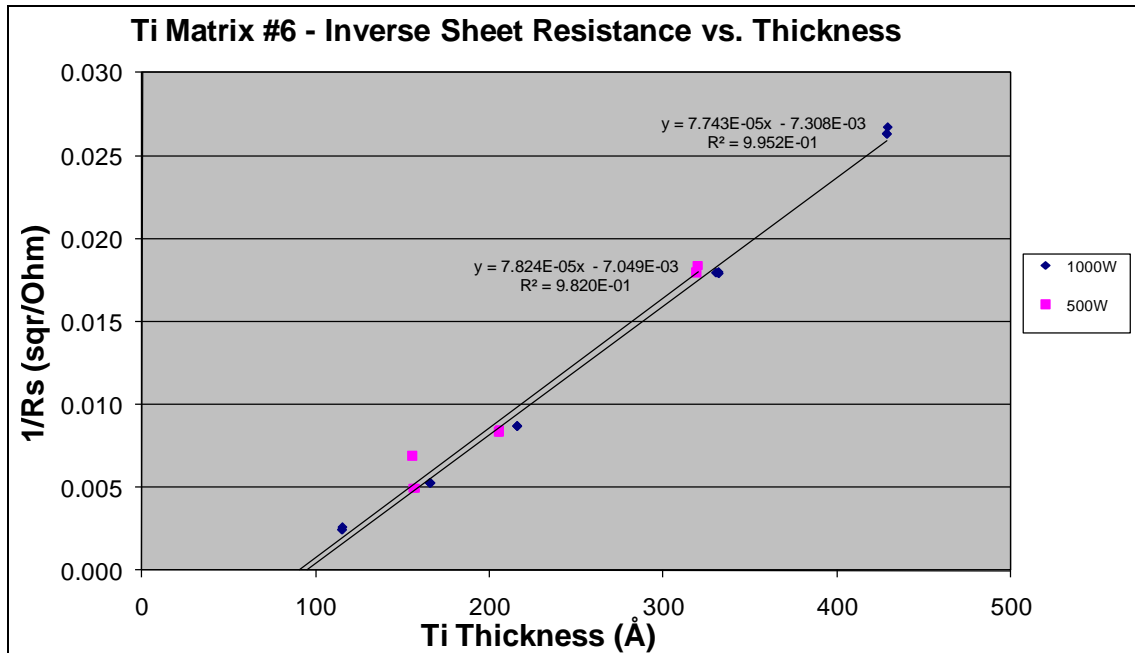


Figure 14. Dependence of $1/R_s$ on Ti thickness for Matrix #6 wafers deposited at 500 W/30 sccm Ar and 1,000 W/30 sccm Ar.

Table 10. Summary of R_s dependence on cathode power, Ar flow rate and deposition time. Slope values can be used to correct deposition conditions to maintain deposition with UL and LL SPC limits.

Deposition Parameter	Slope	Onset Value	Thickness Slope	Thickness Onset
Time (s)	$\Delta(1/R_s)/\text{Unit Power (sq}/\Omega \cdot \text{W})$	Critical Power^* (W)		
19	2.97×10^{-5}	391	NA	NA
95	1.62×10^{-4}	218	NA	NA
Time (s)	$\Delta R_s/\text{Ar Flow Rate } (\Omega/\text{sq}\cdot\text{sccm})$	$\text{Critical } R_s^*$ (Ω/sq)		
19	0.1629	50.3	NA	NA
95	0.0379	6.6	NA	NA
Power (W)	$\Delta(1/R_s)/\text{Unit Time (sq}/\Omega \cdot \text{s})$	Critical Time (s)	$\text{Deposition Rate (nm/s)}$	Critical Time (s)
500	1.79×10^{-2}	10.5	8.48	0.0
1,000	1.27×10^{-3}	4.7	17.46	0.0

*Note that the critical power and critical deposition time are shifted due to the unidentified shift in deposition rate for Ti Matrix #2 and #3.

It should be noted that the linear relationship between $1/R_s$ and thickness is only valid for the small thickness range shown in figure 14 because non-linearity becomes significant over larger thickness ranges. A careful evaluation of the resistivity as a function of film thickness reveals that the resistivity is not constant, as shown in figure 15. The resistivity changes from $470 \mu\Omega\cdot\text{cm}$ at 12 nm to $160 \mu\Omega\cdot\text{cm}$ at 43 nm. There also seems to be a small reduction of resistivity with decreasing cathode power. The trend curve is expected to asymptotically approach the bulk Ti metal resistivity of $40 \mu\Omega\cdot\text{cm}$ as film thickness increases above 100 nm. An

increase in resistivity is commonly observed in thin films due to an increased electron scattering by film surfaces, and increases in strain and defects within thinner films. Differences in porosity/connectivity are also likely to affect the resistivity.

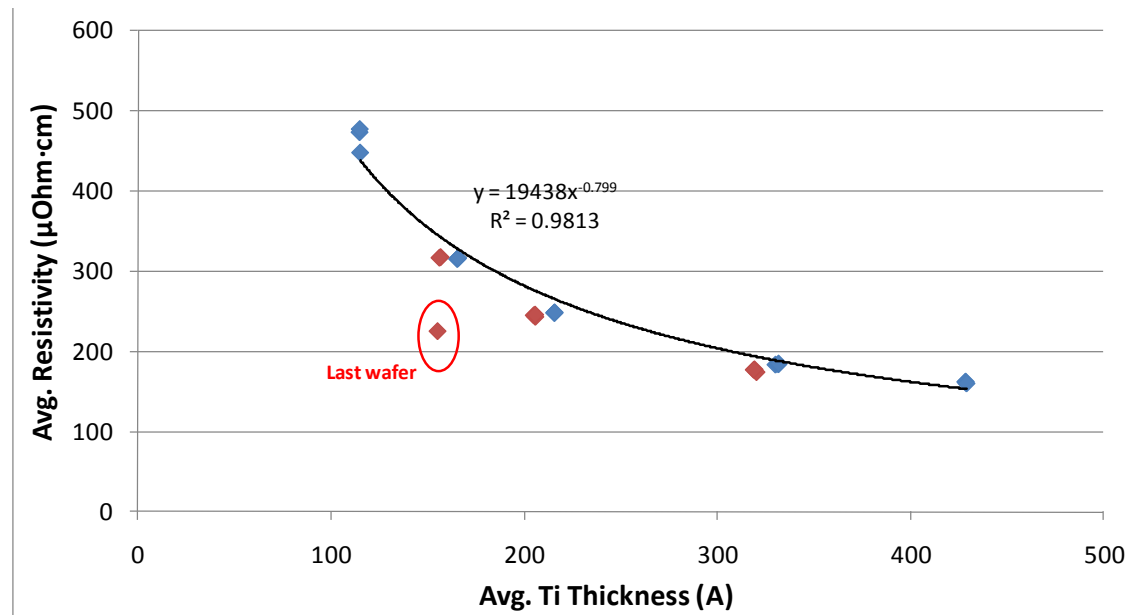


Figure 15. Dependence of resistivity on Ti thickness for Matrix #6 wafers deposited at 500 W/30 sccm Ar and 1,000 W/30 sccm Ar.

The final deposition experiment evaluated for this report was Matrix #5, shown in table 5. This experiment was an attempt to determine whether the wafer supplier or the chamber history was a possible cause for the unexpected shifts in deposition rate observed in the results already reported. Figure 16 gives the R_s values for wafers deposited under the fixed conditions of 1,000 W/30 sccm Ar/19 s on three different days and with different chamber histories prior to deposition. The first six wafers were deposited after the chamber was used to deposit Ti at 500 °C and then cooled to an idle temperature of 42 °C within the same day. The second set of six wafers was deposited after the chamber was idled at 40 °C for 3.5 days. And the third set of six wafers were deposited after a 500 °C Ti deposition and overnight idle that allowed the chamber to cool to 40 °C. Figure 17 provides the TiO₂ thickness results for the three sets of wafers. Two effects are observed from these data sets. Within each set of six wafers, there is a thickness decrease and R_s increase as deposition proceeds from the first to the last wafer. Both the thickness and R_s stabilize after deposition of four to five wafers. This initial effect is consistent with chamber pre-conditioning. A second behavior is observed over the course of the three sets of wafers, namely, an increase in thickness and corresponding decrease in R_s . The cause of this second effect is not clear, but it could potentially be a cause for the unexpected shifts in R_s and thickness between lot runs. It does not explain the shifts that are sometimes observed within a lot or for the last wafer of a lot. There is no apparent difference in the R_s of the films deposited on the two different substrates.

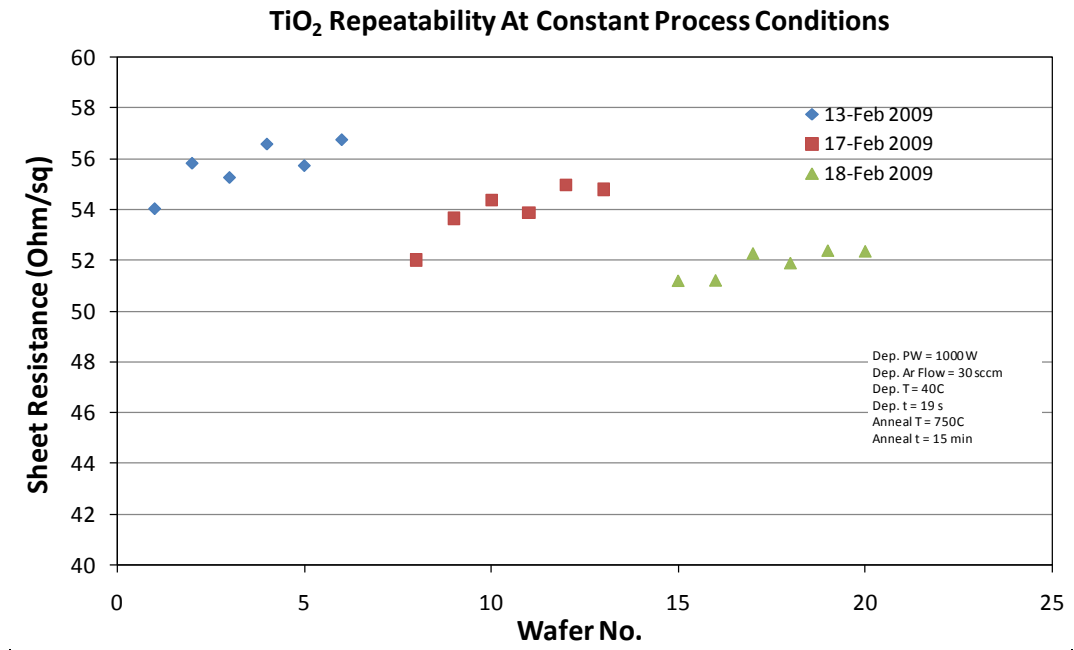


Figure 16. Ti R_s dependence on chamber history for Matrix #5 wafers deposited at 1,000 W/30 sccm Ar/19 s on three different days.

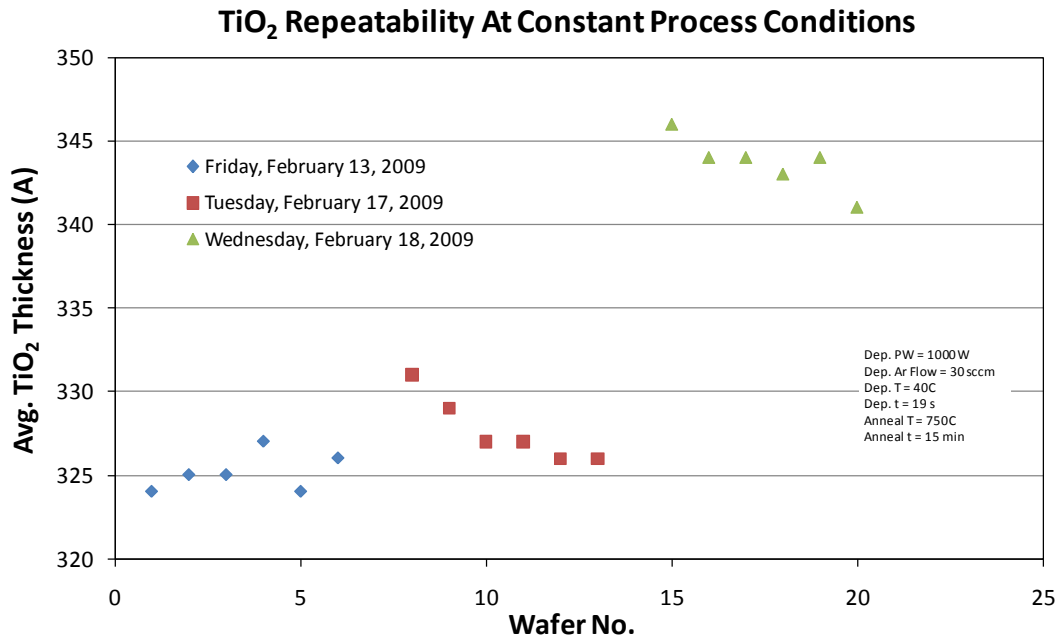


Figure 17. Ti R_s dependence on chamber history for Matrix #5 wafers deposited at 1,000 W/30 sccm Ar/19 s on three different days.

In order to help isolate the intermittent and unexpected shifts in R_s and thickness, the potential sources of instability are summarized as follows.

1. Four-point probe measurement error—This seems unlikely since there is consistency between R_s and ellipsometer-measured thicknesses.
2. Variation in Ar flow or pressure—A pressure-induced shift is unlikely, as described earlier, but cannot be ruled out since relatively large variations in pressure are observed during cathode power up and down.
3. Cathode power instability—A variation of 10 W to 20 W during the entire deposition time could cause the observed thickness and R_s variations. This would also be consistent with the observation that the percentage shift is about the same for different film thicknesses.
4. Deposition time error—A 1-s error is sufficient to cause the observed thickness and R_s variations for 30-nm thick films, but this would not explain why 160-nm films also show a similar percentage shift.
5. Variations in chamber history—Since the number of depositions between lots has a significant effect, it is likely that the chamber history, including pre-sputter conditions, deposition temperature, and pressure history and number of wafers deposited, may affect thickness and R_s instability.
6. Variability in plasma ignition pressure due to poor control of gas stabilization time.

Slowing the deposition rate by instituting a 500-W cathode power and slowing the ramp rate up to the 500-W power level, as currently instituted on the baseline recipe (see section 3.2), may be sufficient to eliminate the R_s and thickness instabilities, but continued PCM evaluation is needed to confirm elimination of this problem.

3.2 Ti, and TiO₂ Thin Film Crystallography

A basic analysis of the crystallography of Ti, TiO₂, and Pt films was completed by collecting a θ -2 θ scan of samples representative of each deposition condition. A spectrum for a Ti thin film deposited at 500 W/30 sccm Ar/24 s/18–21 °C, with the heater disabled and having R_s = 89.9 Ω/sq, is shown in figure 18. Since the X-ray penetration depth is approximately 1 μm, and the Ti and SiO₂ layers are only 0.5 μm thick, a strong 400 Si peak is obtained by diffraction from the 100 Si substrate (ICDD card #27-1402). A diffraction peak resulting from W_{La} characteristic radiation is also obtained because of incomplete filtering by the monochromator. In a standard Si diffraction pattern, the Si 200 peak is forbidden due to crystallographic symmetry; but in figure 18, the Si 200 peak is observed due to the strain introduced by the films grown on the surface of the substrate. It should be noted that the intensities of the Si peaks will vary considerably according to the alignment of the Si substrate within the diffractometer sample holder, and the strain of the wafer caused by surface films and processing conditions.

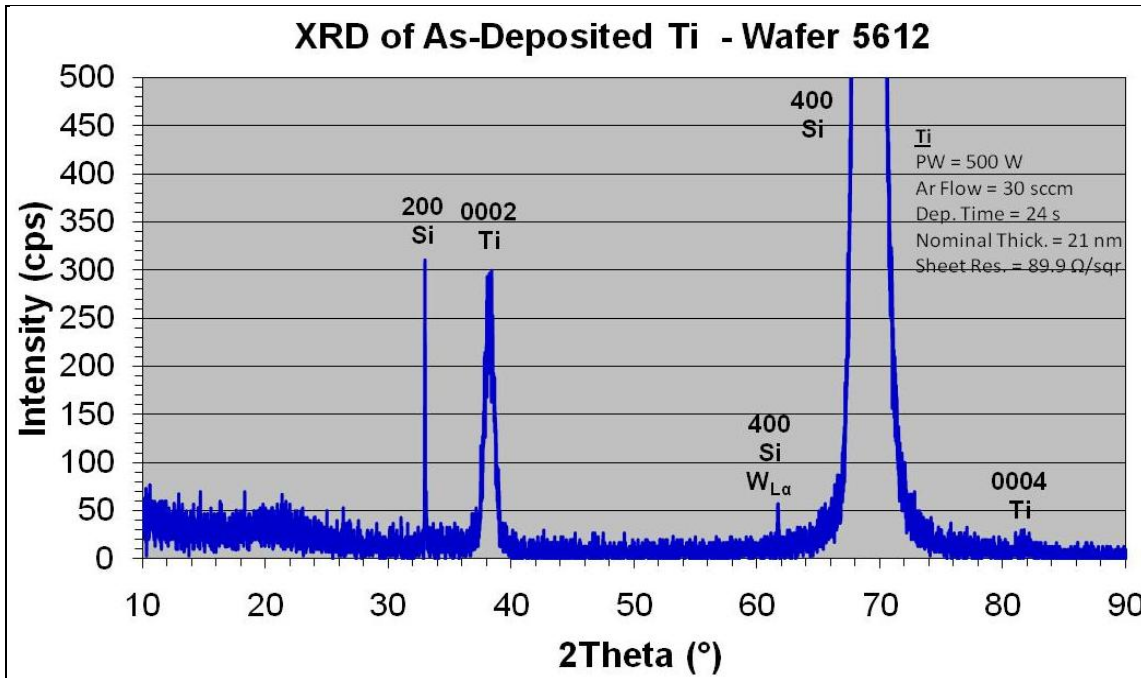


Figure 18. XRD 0-2θ scan of an as-deposited Ti film confirming {0001}-texture.

Figure 18 shows only two peaks, the 0002 and 0004, characteristic of the Ti film (ICDD card #44-1294). Since only 0001 reflections are observed, it can be concluded that the film is strongly {0001} textured. Although the as-deposited Ti films were not regularly characterized by XRD, it is expected that figure 18 is typical of the XRD patterns that would be obtained from Ti-coated wafers. The wafer-to-wafer repeatability was confirmed to be within the XRD measurement error by measuring a second wafer coated with Ti under the same deposition conditions. Within the range of deposition conditions investigated, it is assumed that only small peak shifts in 0001 peak positions intensities and FWHM occur between samples, although this has not yet been confirmed experimentally. We also expected that the tilt distributions of the textured Ti grains, as determined from rocking-curve measurements, will vary with deposition conditions. Studies of the relationship between the Ti deposition parameters and the Ti texture are recommended for future studies for the optimization of electrode texture. The study presented here focused on finding a combination of Ti deposition and oxidation anneal conditions that resulted in a baseline {200}-textured TiO₂ template for {111}-textured Pt growth and enhanced electrode temperature stability. It is conjectured that the {0001}-texture distribution of the Ti film determines the ultimate TiO₂ {200}-texture distribution that can be achieved via oxidation annealing. The following data indicate that Ti texture is but one factor contributing to the final TiO₂ texture quality.

An example diffraction pattern of a TiO₂ film is shown in figure 19. The TiO₂ film was formed by oxidizing the sputter-deposited Ti films with an O₂ anneal in a tube furnace. During annealing in the 650–800 °C range, oxygen diffuses into the Ti film. It appears that the original Ti {0001}-

texture is maintained and that the oxygen merely stuffs the Ti lattice to form the rutile structure TiO_2 film with a $\{200\}$ -texture. The effect of the anneal temperature and time on the TiO_2 structure can be determined from the quantitative XRD results shown in figures 20, 21, and 22. In figure 20, it is observed that the 200 peak position reaches a plateau of approximately 39.45° (20), and the FWHM reaches a minimum of approximately 0.39° between 750 – 800 °C. As a consequence, the maximum peak intensity maximizes within the same temperature range, and it is clear that a 30-min anneal results in a higher intensity than a 15-min anneal at the corresponding temperature. These results indicate that the TiO_2 film reaches a stable strain state, minimum strain inhomogeneity, and maximum density in the 750 – 800 °C anneal temperature range. The RC-FWHM values plotted in figure 22 confirm that the TiO_2 maintains texture through the oxidation anneal and $\{100\}$ -texture is maximized (RC-FWHM minimized) in the 750 – 800 °C anneal temperature range. From the combination of results presented in figures 20, 21, and 22, it can be concluded that the TiO_2 film annealed at 750 °C for 30 min will provide an optimized template for $\{111\}$ -textured Pt growth and will also remain stable at anneal temperatures used for PZT crystallization. Higher TiO_2 anneal temperatures could be used, but are not necessary and would be detrimental if the process were integrated with wafers containing CMOS circuitry.

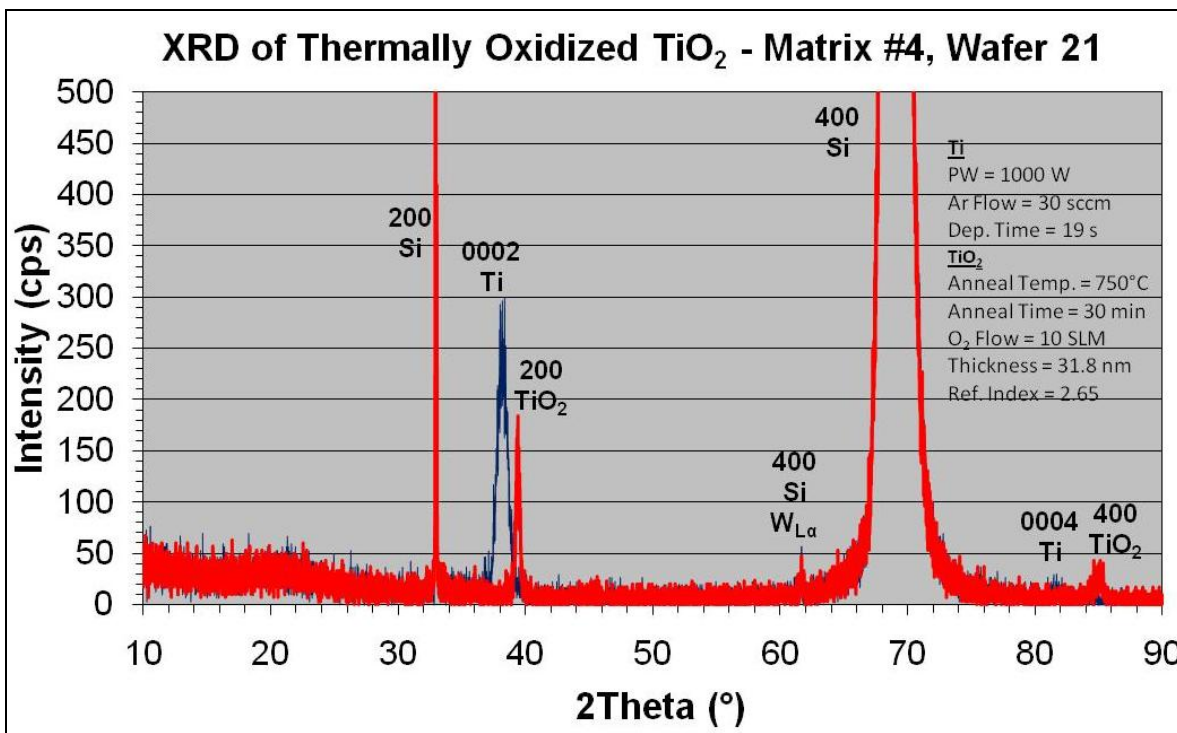


Figure 19. XRD 0-2θ scan of TiO_2 film confirming $\{100\}$ textured rutile structure and comparison with as deposited $\{0001\}$ texture Ti film. The Ti and TiO_2 film details are given for the Matrix #4/Wafer 21 sample for which the XRD pattern is displayed in red.

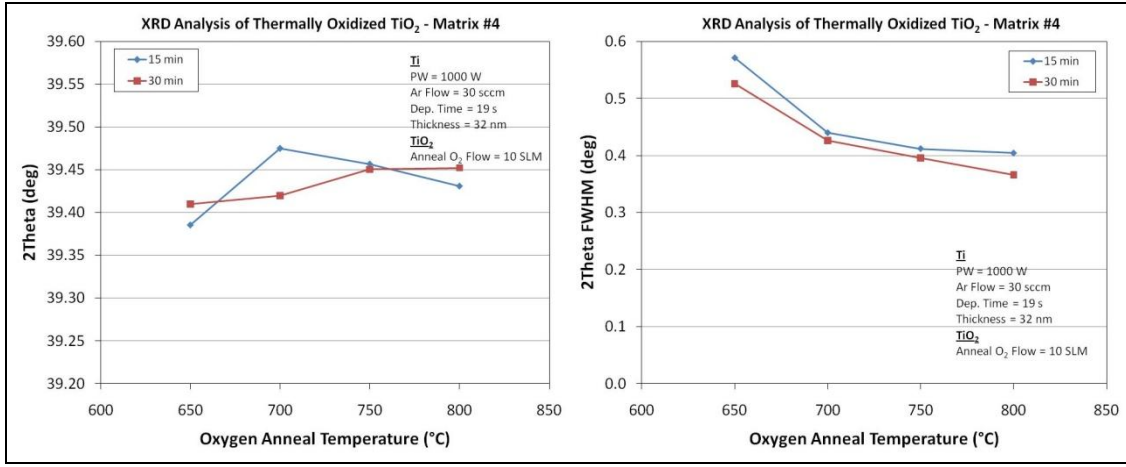


Figure 20. Comparison of the 200 rutile XRD peak positions and intensities for TiO₂ films formed by oxidation annealing between 650 and 800 °C.

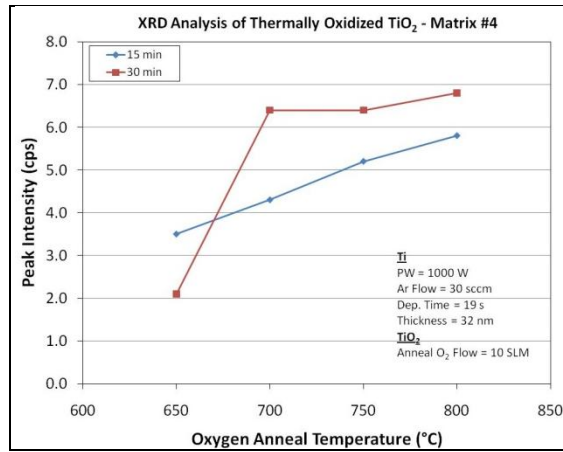


Figure 21. Comparison of the 200 rutile XRD peak FWHM for TiO₂ films formed by oxidation annealing between 650 and 800 °C.

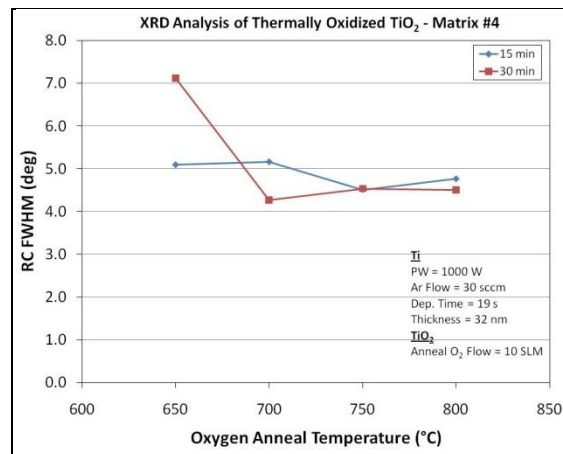


Figure 22. TiO₂ Rocking-curve FWHM dependence on anneal temperature and time.

An analysis of the effect of Ti thickness and deposition power on the formation of TiO_2 and subsequent growth of Pt was completed by using Ti films from Matrix #6 and a constant annealing condition of $700\text{ }^\circ\text{C}/10\text{ SLM O}_2/15\text{ min}$. It should be noted that this condition is not the recommended optimum anneal condition of $750\text{ }^\circ\text{C}/10\text{ SLM}/30\text{ min}$ determined from the completed TiO_2 analysis. We believe that the TiO_2 formation was close enough to the optimum anneal condition to validate the general trends reported as a function of Ti/ TiO_2 thickness and Ti deposition power. As expected, the 200 TiO_2 peak intensity increased with increasing Ti film thickness (increasing deposition time). We also found that the peak intensity increased and the RC-FWHM decreased for films deposited at 500 W when compared with films deposited with the same thickness at 1,000 W. These results are consistent with the general behavior for sputtered thin films that are deposited with reduced deposition rate and reduced sputtered ion energies (8–12).

3.3 Pt Thin Film Crystallography and Effect of TiO_2 Seed Layer

Following the analysis of the annealed TiO_2 films, Pt was deposited onto a series of $\text{Ti/SiO}_2/\text{Si}$ wafers chosen from Matrix #6. The TiO_2 films were randomly ordered and coated with 100 nm Pt in the Oerlikon Clusterline sputtering chamber #4 using a substrate temperature of $500\text{ }^\circ\text{C}$, Ar flow rate of 50 sccm (5×10^{-3} mbar), and DC cathode power of 500 W, and analyzed by XRD. The sheet resistivity, R_s , of the Pt fell into the range of $1.25\text{--}1.26\text{ }\Omega/\text{sq} \pm 0.2\text{ }\Omega/\text{sq}$ standard deviation for these Pt samples with no clear trend of Pt resistivity increase with increased TiO_2 thickness. The Pt appears to have random variations in resistivity of approximately $0.03\text{ }\Omega/\text{sq}$.

Looking at figure 23 for Matrix #6, we see that both the 200 and 400 TiO_2 peak heights increase and the FWHM decreases for the 500 W RF Ti-deposition power. This increased texture is confirmed by the FWHM of the 200 TiO_2 rocking curve data shown in figure 24. Peak positions of the 400 TiO_2 are slightly larger by approximately 0.5 degrees for 500 W than for 1,000 W, indicating larger stress relative to 84.2577 for the unstressed case, but at both power levels the stress decreased with increasing TiO_2 thickness. A clear trend like this could not be seen in the peak position for the 200 TiO_2 peak and rocking curve position data (perhaps due to greater impact of noise on peak and rocking curve data at the lower diffraction angle).

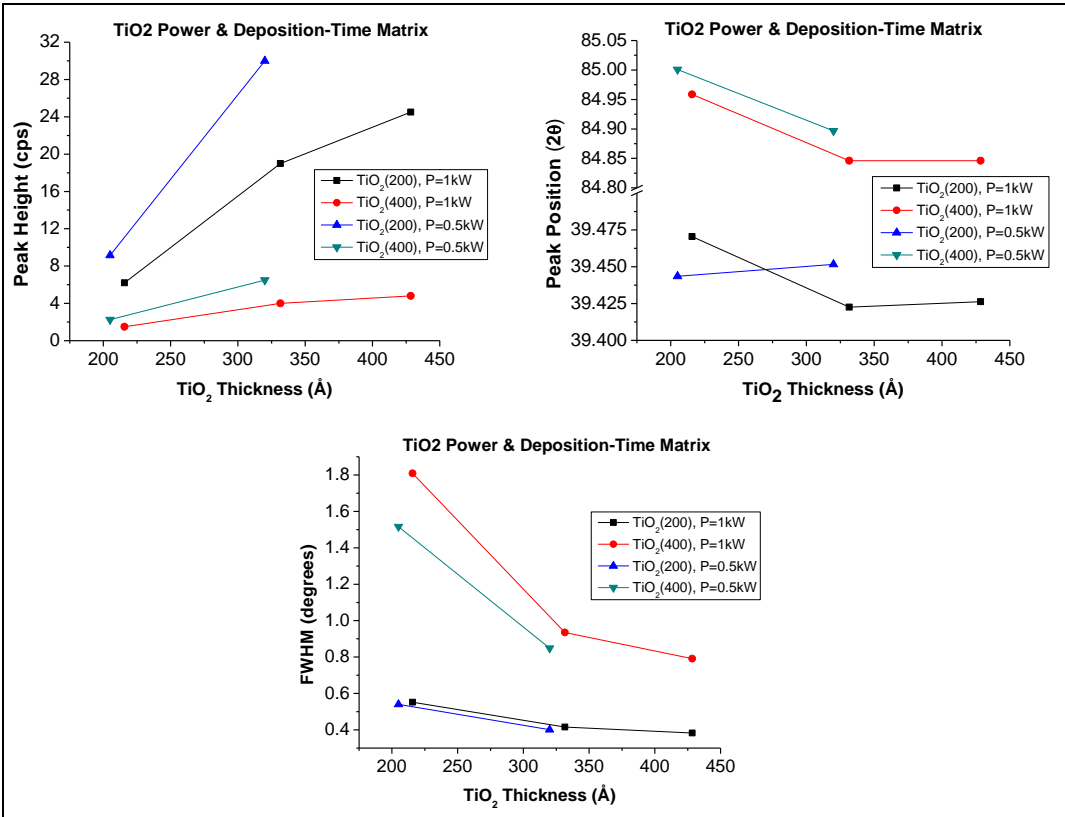


Figure 23. Comparison of the 200 rutile XRD peak positions, intensities, and FWHM for TiO₂ films 20–42.5 nm thick deposited at 500 or 1,000 W.

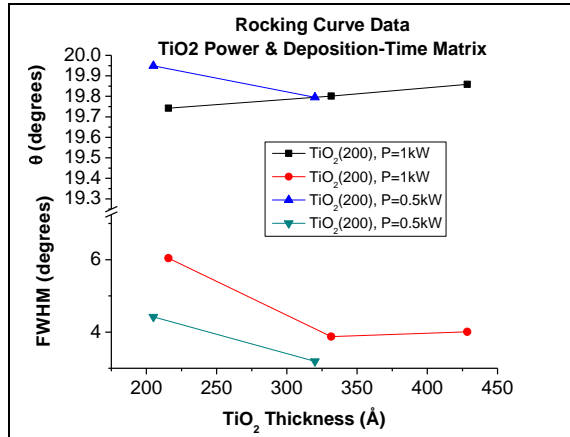


Figure 24. TiO₂ Rocking Curve FWHM and position dependence on deposition thickness and RF power.

Figure 25 shows the relative positions of the 0002 Ti, 200 TiO₂, and 111 Pt peaks. The relatively large intensity of the Pt peaks lowered the S/N appreciably, increasing the accuracy of the Pt peak analyses.

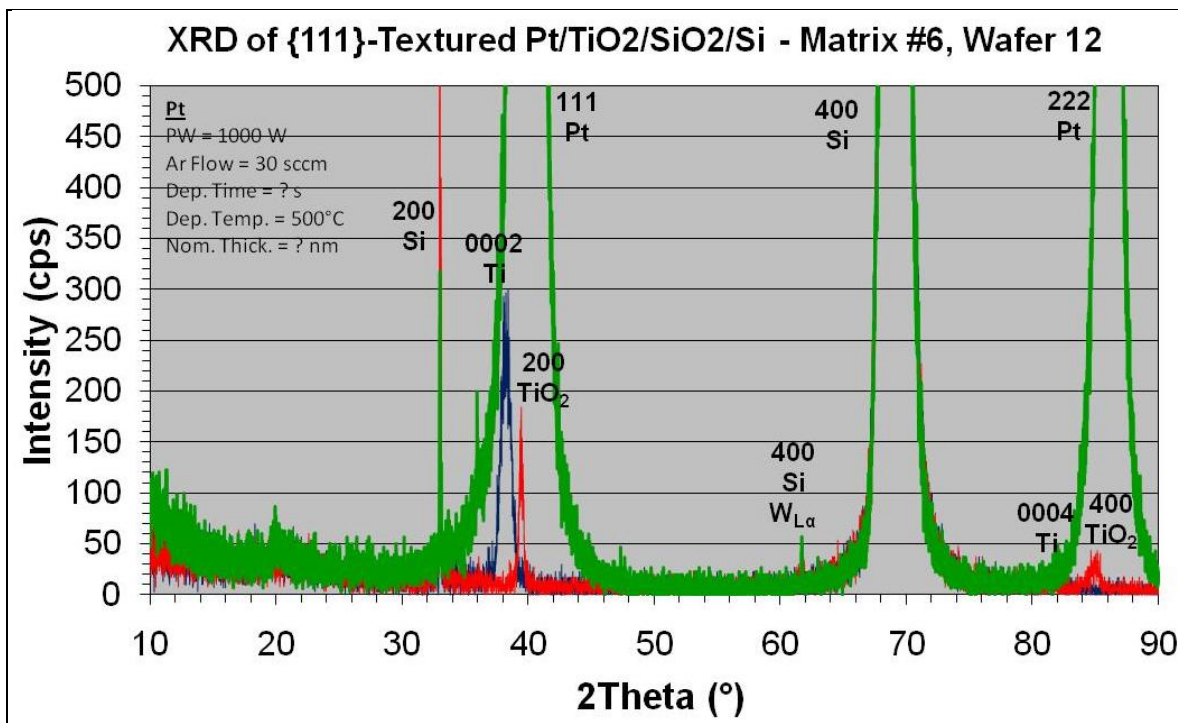


Figure 25. Comparison of XRD 0–2θ spectrum for {111}-textured Pt, {100}-textured TiO₂ seed layer and as-deposited {0001}-textured Ti film.

Figure 26 correlates the Pt 111 and 222 peak intensity and FWHM to that of TiO₂ 200 and 400, respectively. Similar data is shown for 111 Pt and 200 TiO₂ rocking curve data. The results show a clear trend of increasing Pt intensity and lowering of the Pt FWHM for the 500 W Ti deposition relative to 1,000 W Ti RF-power deposition. A clear correlation between the {100}-textured TiO₂ and {111}-textured Pt is observed, proving that the TiO₂ acts as a seed layer for the Pt.

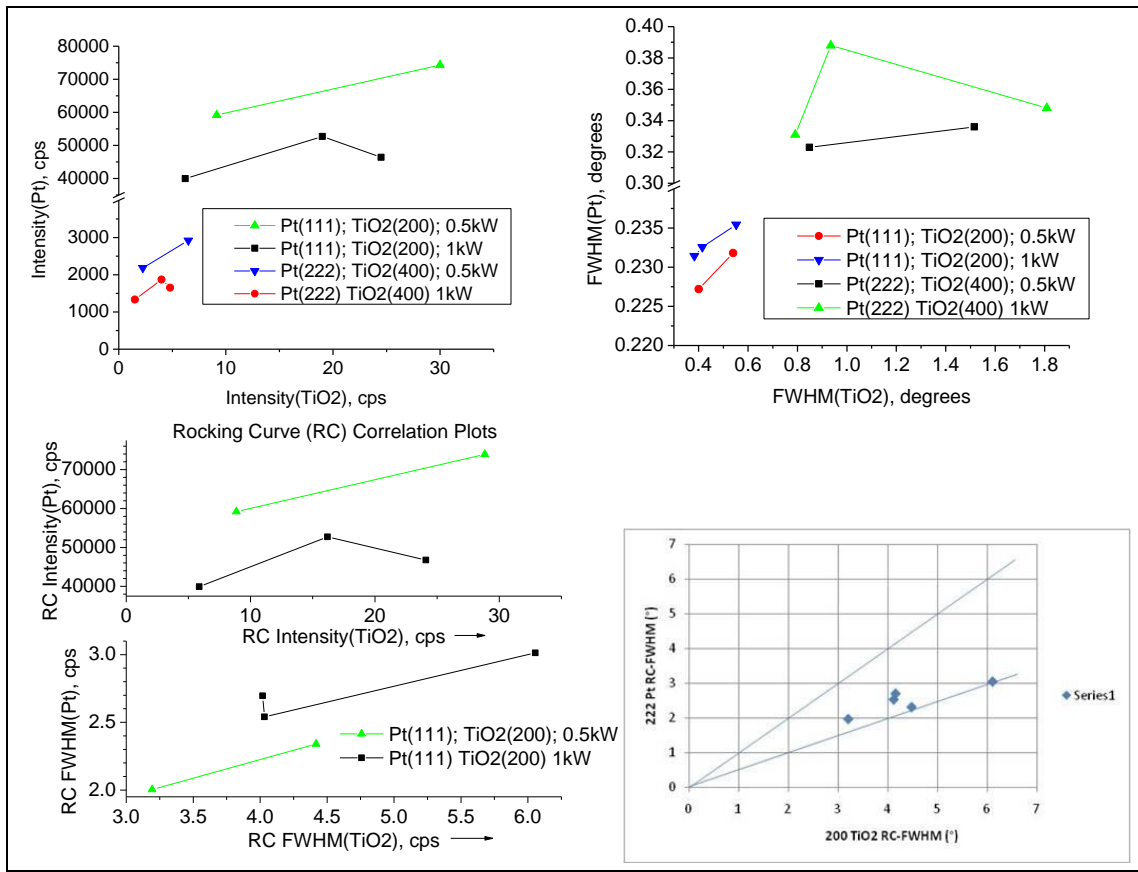


Figure 26. Correlation of Intensity and FOM XRD for Pt vs. TiO₂.

Also included in figure 26 is a plot of 222 Pt versus 200 TiO₂. It shows the general trend with five data points. It can be seen that the Pt 222 RC-FWHM increases linearly with increasing TiO₂ 200 RC-FWHM. The relationship should have a slope of 1 for the ideal case, but it has a slope closer to 0.5. The trend is valid, though it's not clear whether the slope has an issue with the measurement or with some factor in the relationship.

An extension of the Pt intensity and FWHM data over an extended TiO₂ film-thickness regime for deposition power equal to 500 W is shown in figure 27. These results show that the optimum deposition thickness has a range of roughly 35–40 nm, corresponding to a deposition time range of about 40–50 s. This data was taken only recently in 2010, and just prior to that, the X-ray tube had just been replaced. Therefore, the intensities are much larger than for the other measurements shown in this report.

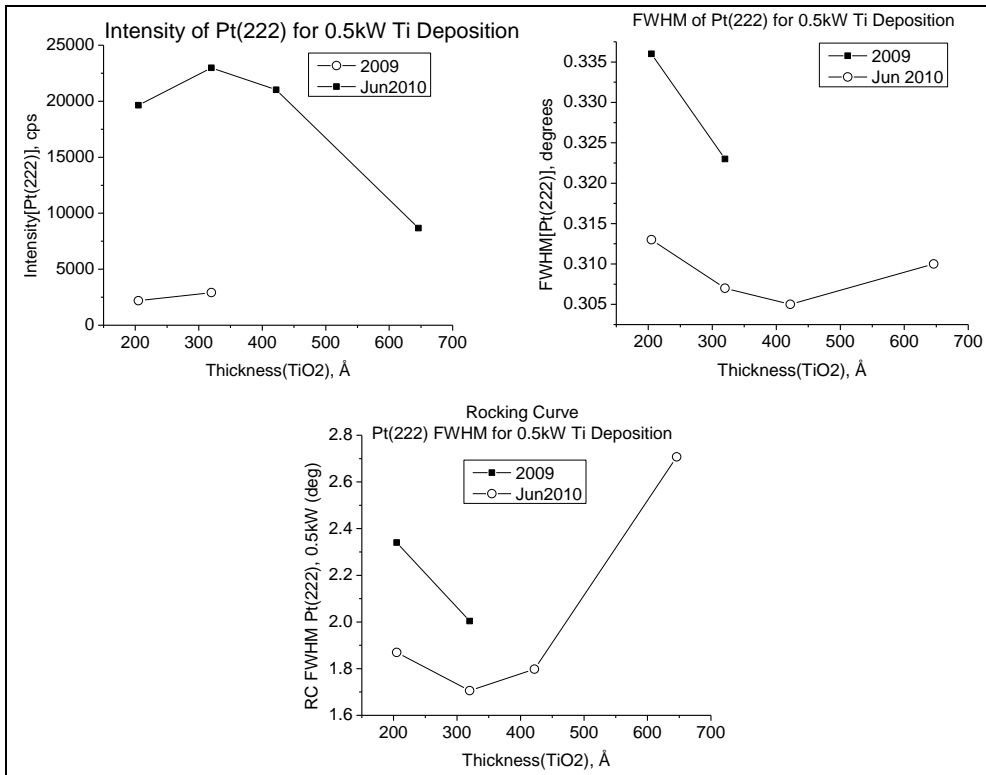


Figure 27. Extended thickness range of Pt(222) XRD for peak intensity, peak FWHM, and rocking-curve FWHM.

In figure 28, the peak intensity and FWHM results for 111 Pt (Process #2: Matrix #6 Wafer #18 90–100 nm Pt, 500 °C, 30 sccm Ar deposition, which included Ti deposition at 500 W, 38 s, 40 °C, 30 sccm Ar, and Ti oxygenation anneal at 700 °C/15 min/10 SLM O₂, obtaining 32 nm TiO₂) were compared with those for a Pt film processed using the standard ARL recipe for TiO₂ and Pt processes prior to these studies (Process #1) and to state-of-the-art Pt samples, Processes #3 and #4, obtained from NIST. All of the Pt XRD measurements were made under identical circumstances and for similar Pt thicknesses of about 100 nm. The results show good improvement of the process due to the improvements in the TiO₂ process, which are expected to further improve for longer (40–50s) Ti-deposition times with 750 °C Ti oxygensations. In addition, preliminary results indicate improved 111 PZT orientation on the PTO seed layer using wafers platinized using this new process, compared to PZT deposited using the old process. Figure 29 shows XRD for the new PZT superimposed onto those of the textured Pt and TiO₂.

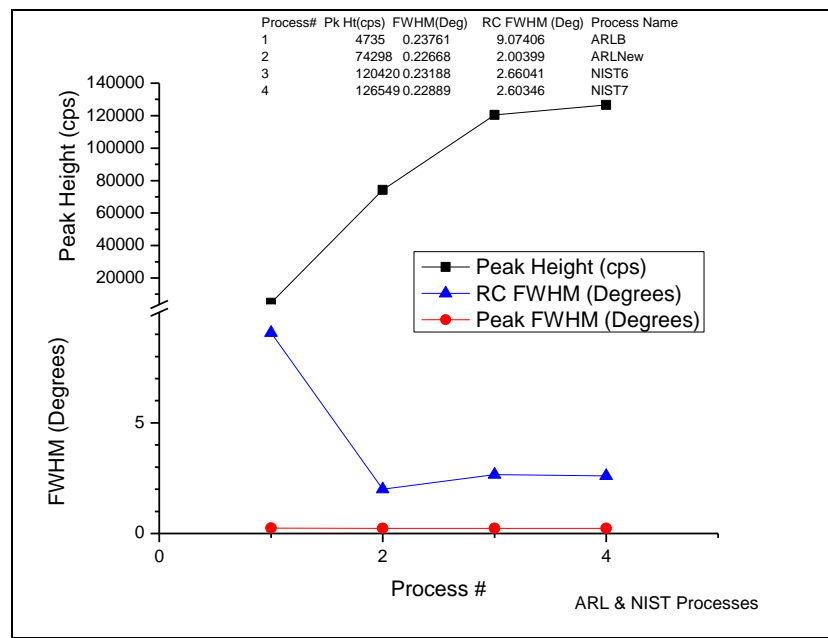


Figure 28. Comparison of Pt(111) process (#2) to prior ARL (#1) and NIST (#3 & #4) processes.

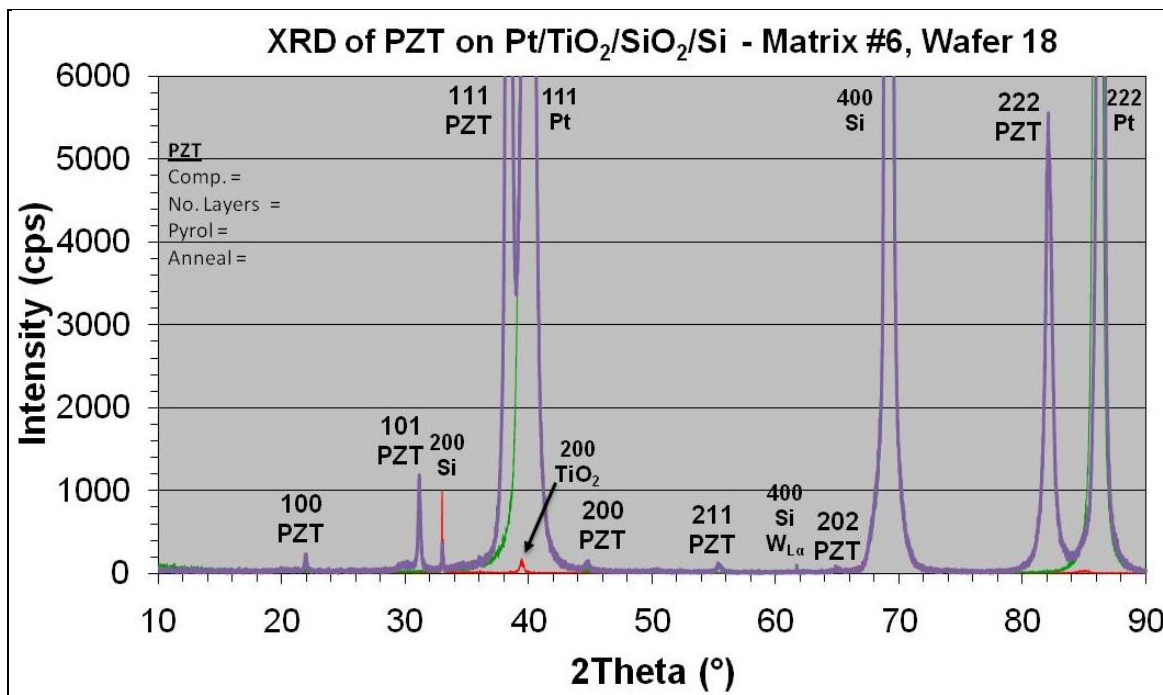


Figure 29. Comparison of XRD 0-2θ spectrum for {111}-textured Pt, {100}-textured TiO₂ seed layer and highly {111} textured PZT.

4. Conclusion

Analysis of the 222 Pt XRD peak shows that peak height is maximized and FWHM is minimized for a TiO₂ film thickness of approximately 30 nm. Compared with the baseline Pt on Ti electrode process used at ARL, the optimized Pt on TiO₂ process exhibits nearly an 8-fold improvement in the 222 Pt peak height and a decrease in rocking curve FWHM for 9° to 2°. Use of the Pt on TiO₂ electrode for growth of PZT(52/48) results in films with an estimated {111} textured volume fraction of 90% compared with the nearly 100% random PZT orientation obtained on the baseline Pt on Ti electrode. The increased {111} texture is expected to result in improved electrical properties of the PZT films. The peak height and rocking curve FWHM values for the new ARL Pt process though quite improved are still not the most optimal Pt deposition conditions because evidence shows that the process would further benefit from an increase in the Ti oxidation anneal temperature from 700–750 °C and from a longer Ti deposition time to somewhere in the range of 40–50 s. The Pt process change improves the PZT texture and has been introduced as a Pt module for the MEMS Exchange with the currently-defined process (appendix B) and competitive pricing and throughput estimates for production in the ARL cleanroom facility (appendix C).

5. References

1. Vaudin, M. D.; Fox, G. R.; Kowach, G. R. Accuracy and Reproducibility of X-ray Texture Measurements. *Mat. Res. Soc. Symp. Proc.* **2002**, *721*, J1.2.1–J1.2.6.
2. Chu, F.; Fox, G.; Enstep, B. Multi-Layer Approach for Optimizing Ferroelectric Film Performance. US Patent #6,287,637 B1, September 11, 2001.
3. Chu, F.; Fox, G. Method for Manufacturing a Ferroelectric Memory Cell including Co-annealing. US Patent #6,376,259 B1, April 23, 2002.
4. Fox, G.; Chu, F.; Eastep, Brian; Takamatsu, Tomohiro; Horii, Yoshimasa; Nakamura, Ko. Process for Producing High Quality PZT Films for Ferroelectric Memory Integrated Circuits. US Patent #6,887,716 B2, May 3, 2005.
5. Calame, F.; Muralt, P. Growth and Properties of Gradient Free Sol Gel Lead Zirconate Titanate Thin Films. *Appl. Phys. Lett.* **2007**, *90* (6), 062907.
6. Herzinger, C. M.; Johs, B.; McGahan, W. A.; Woollam, J. A. Ellipsometric determination of Optical Constants for Silicon and Thermally grown Silicon Dioxide via a Multi-sample, Multi-wavelength, Multi-angle Investigation. *J. Appl. Phys.* **1998**, *83*, 3323.
7. *Handbook of Optical Constants of Solids*; E.D. Palik (ed.), Academic: New York, Vol. 1, p. 759.
8. Douglass, D. L.; Van Landuyt, J. The Structure and Morphology of Oxide Films During the Initial Stages of Titanium Oxidation. *Acta Metallurgica* **1966**, *14*, 491.
9. Hoshi, Y.; Suzuki, E.; Shimizu, H. Control of Crystal Orientation of Ti Thin Films by Sputtering. *Electrochimica Acta* **1999**, *44*, 3945.
10. Jung, M. J.; Nam, K. H.; Shaginyan, L. R.; Han, J. G. Deposition of Ti Thin Film Using the Magnetron Sputtering Method. *Thin Solid Films* **2003**, *435*, 145.
11. Lugomer, S.; Stipancic, M.; Persin, A. In Situ MBI Reflection Observation of Thin Ti Film Oxidation. *Appl. Optics* **1983**, *22* (21), 3314.
12. Ting, C.-C.; Chen, S.-Y.; Liu, D.-M. Preferential Growth of Thin Rutile TiO₂ Films Upon Thermal Oxidation of Sputtered Ti Films. *Thin Solid Films* **2002**, *402*, 290.

Appendix A. Rigaku Diffractometer Setup & XRD SPC for TiO₂ Adhesion Layer

Purpose: XRD measurement for statistical process control of the TiO₂ adhesion layer.

1. Tool Configuration

- Tool Name: Rigaku D/Max 2200PC Ultima III
- Tool Description: θ - 2θ X-ray Diffractometer with interchangeable Bragg-Brentano and Parallel Beam configurations

2. X-ray Source: sealed Cu anode tube, 2.2 kW, long fine line

- Vender Name: ATPS, INC (Advanced Technical Products & Services)
- Address: P.O. Box 424, Douglasville, PA 19518
- Telephone: 610-689-4540 (FAX: 610-489-1641)
- Email: info@atpsinc.com (Web: atpsinc.com)
- Model No.: ATPS XRD 1000 60-12 Cu L, long fine focus, W2200, S/N 133416
- Typical Delivery Time: Immediate ARO
- Typical Lifetime: Replace tube after about 5k–10k hr (100% Warranty up to 2,500 h)
- Tube Power Settings: 40 kV, 44 mA
- Incident Radiation: CuK α 1, CuK α 2, CuK β , WL α , bremsstrahlung, 4 mm width at 90 deg, 23 mm high

3. Optics Configuration: Bragg-Brentano

- Position #1: Empty Beam Path Assembly
- Position #2: Bragg Brentano Slit
- Position #3: 5° Axial Divergence Collimator, also called the incident beam solar parallel slit assembly
- Position #4: 10 mm, H10, Height Limiting Slit placed in top slot of divergence slit assembly
- Position #5: Detector Box Optic
- Position #5a: forward filter holder position = empty
- Position #5b: 5° Axial Divergence Collimator, also called receiving beam solar parallel slit assembly, parallel foils vertically oriented
- Position #5c: empty
- Position #5d: aft filter holder position = empty
- Position #6: monochromator crystal inserted with "BENT" label facing forward
- Monochromator Type: graphite.
- Monochromator Output Wavelength: CuK α (does not resolve α 1 and α 2)
- Position #7: monochromator receiving slit (see measurement procedure)

- Position #8: scintillation detector, linear response from 0 to 100,000 cps (700,000 if counting loss correction is completed)
- Tube-to-Sample Radius: R_{tube} = 285 mm
- Sample-to-Detector Radius: R_{det} = 285 mm

4. Tool Vender Information

- Tool Supplier: Rigaku Americas Corporation
- Website: www.rigaku.com
- Address: 9009 New Trails Dr., The Woodlands, TX 77381-5209
- Telephone: 281-362-2300
- Fax: 281-364-3628
- Sales Contact: Sean Bird, Tom Concolino
Email: sean.bird@rigaku.com, tom.concolino@Rigaku.com
Telephone: 919-557-8326
Address: 6013 Brass Tack Ct., Fuquay-Varina, NC 27526
- Service Contact: Service Help Desk
Telephone: 888-362-2324 or 281-362-2300 x132
Email: support@rigaku.com

5. Alignment Check Procedure - Alumina Standard (complete daily)

- Warm-Up X-ray Source: 30 min at 40 kV/44 mA
- Standard Type: 96% Al₂O₃, corundum structure, polycrystalline (Coorstek 99.5–99.6%)
- Diameter: 100 mm wafer
- Thickness: 500 μm
- Description: polished one side, (CoorsTek: flatness $\pm 0.0005''/\text{inch}$, parallelism 0.0005")
- Part No.: 52067 (CoorsTek)
- Vender Name: CoorsTek
- Address: Golden, CO
- Telephone: 800-821-6110 (FAX: 303-271-7009)
- Website: coorstek.com
- Sample Placement: flat toward back of fixed, spring clip sample holder - use aluminum plate behind sample to ensure sample is firmly held against top surface of sample holder.
- XRD optics Position #7: monochromator receiving slit = largest or none (confirm that intensity is <100,000 cps)
- Scan Type: θ -2 θ
- Scan Rate: 1.0 deg/min
- Step Size: 0.01 deg.
- 2 θ Range (deg.): 24–27, 56–59, 94–97
- Target Values: ± 0.01 deg, $\pm 5\%$ cps
- Peak 012: 25.5835 deg. / 75% cps
- Peak 116: 57.5177 deg. / 80% cps

- Peak 226: 95.2597 deg. / 14% cps
- Total Scan Time: 9 min

Note#1: Include software setup and Rigaku alignment for zero degree and other tests for best results.

Note#2: Do a series of measurements to establish actual target values

Note#3: Shifts in peak positions indicate misalignment or sample height offsets.

Note#4: Track intensity over time to monitor tube lifetime.

Note#5: Sudden changes in intensity indicate misalignment, change in optics configuration, incorrect slits or filters.

6. TiO₂ XRD Setup Procedure

6.1 θ-2θ characterization measurement (optional).

- Warm-Up X-ray Source: 30 min at 40 kV/44 mA
- Sample Type: whole wafer, partial wafers can be used if they are larger than the beam area
- Diameter: 100 mm wafer
- Thickness: 30 nm thin film
- Description: Sputtered Ti oxidized at ≈ 750 °C, 30 min.

Sample Placement: flat toward back of fixed, spring clip sample holder, must define 1,3 and 5 - site measurement positions and mounting

- XRD optics Position #7: monochromator receiving slit = largest or none (confirm that intensity is <100,000 cps)
- Scan Type: θ-2θ
- Scan Rate: 2.0 deg/min
- Step Size: 0.02 deg.
- 2θ Scan Range (deg.): 10–90
- TiO₂ SPC Procedure - includes θ-2θ and θ (rocking curve) measurements.
- Warm-Up X-ray Source: 30 min at 40 kV/44 mA
- Sample Type: whole wafer, partial wafers can be used if they are larger than the beam area
- Diameter: 100 mm wafer
- Thickness: 30 nm thin film
- Sample Placement: flat toward back of fixed, spring clip sample holder, must define 1,3 and 5 - site measurement positions and mounting
- XRD optics Position #7: monochromator receiving slit = 0.6 mm (Baseline Calibration: Pt(111) for Ti Oxidation: 750 °C, 30 min, 11/13/09 Pt: 100 nm, 500 °C, 12/10/09, continuous scans at 0.02 deg, 0.1deg/min, Counts \approx 400,000 cps)
- Scan Type #1: θ-2θ
- Scan Rate: 1.0 deg/min

- Step Size: 0.01 deg.
- 2θ Scan Range (deg.): 38–41
- Target Values: ± 0.01 deg, $\pm 5\%$ cps
- Peak 200: 39.1866 deg. / 35 Cps / 0.5 deg FWHM
- Total Scan Time: 20 min

6.2 Scan Type #2: θ

- Scan Rate: 1.0 deg/min
- Step Size: 0.01 deg.
- θ Scan Range (deg.): 5-35
- Target Values: ± 0.01 deg, $\pm 5\%$ cps
- Peak 200: 19.6 deg. / 35 cps / 5 deg FWHM
- Total Scan Time: 30 min

7. Tool Usage

- Avg. Usage Time (per month): 40-160 h
- Avg. Maintenance Time (per month): 25 h (mainly calibration checks)
- Avg. Training Time (per month): 8 h
- Avg. Idle Time: (per month): 560-680 h (includes overnight & weekends)

Reference Documents

1. BOG-U3-v2.pdf: Rigaku D/Max 2200PC Ultima III Basic Operations Guide, Manual No. BOG-U3-v2, February 2006
2. BB & PB Rigaku Ultima III Setup.pdf: scan of hand sketch
3. GF_TiO2 Pt XRD SPC_6-24-09.ppt: TiO2 and Pt XRD Measurements

Appendix B. Currently-defined Process Recipe

Ti Deposition

- Chamber condition to 40 °C
- Dummy deposition time = 1800 s
- Ti deposition at 40 °C, 24 s, Power = 500 W

Ti oxidation

- 750 °C, 30 min, flowing O₂

Pt Deposition

- Chamber condition to 500 °C
- Dummy deposition time = 300s
- Pt deposition at 500 °C, 100 nm, Power = 1,000 W

INTENTIONALLY LEFT BLANK.

Appendix C. Pt module for MEMS Exchange

Data includes estimates for production in the ARL clean-room facility and competitive pricing.
Select thickness for Pt only.

($\text{SiO}_2 = 500 \text{ nm}$ & $\text{TiO}_x = 20 \text{ nm}$ will remain fixed)

Example Pt Thicknesses: 100.0 nm, 200.0 nm.

Specify batch size (Example batch: 25 wafers).

Selected material = Pt.

100 mm Silicon Substrates ready for PZT or other specialty film depositions. The wafers include the following films:

Pt Top Layer:

Sputter-deposited: 2 h, 4 h 25-wafer batch process plus 15 min target preparation time

Thickness = $100 \text{ nm} \pm 20 \text{ nm}$ OR $200 \text{ nm} \pm 20 \text{ nm}$

Sheet Resistance $< 2 \Omega/\text{sq}$

Orientation = $<111>$ normal to substrate surface

111 Rocking Curve FWHM < 5 degrees (θ) (CuK α 1 radiation)

TiO₂ Template Layer:

Sputter-deposited: 2 h 25-wafer batch process plus 15 min target preparation time

High-temperature furnace annealed 4 h batch process

Orientation = $<200>$

Thickness = 32 nm – 35 nm

SiO₂ Layer:

Thermal oxidation of Si Substrate – vendor supplied

Thickness = $500 \text{ nm} \pm 20 \text{ nm}$

Si Substrate:

Vendor supplied

Prime wafer

Diameter = 100 mm

Flat = Semi-standard

Thickness = $500\text{-}550 \mu\text{m}$

Resistivity = 1-30 $\Omega\text{-cm}$

Orientation = $<100>$

Pricing Option 1

Pt(100 nm) / TiO_x (20 nm) / SiO₂ (500 nm) / Si ARL

Cost: \$164.00/wafer

Pricing Option 2

Pt(200 nm) / TiO_x (20 nm) / SiO₂ (500 nm) / Si ARL

Cost: \$192.25/wafer

List of Symbols, Abbreviations, and Acronyms

ARL	U.S. Army Research Laboratory
Cu	copper
FRAM	Ferroelectric Random Access Memory
FWHM	full width at half maximum
ICDD	International Centre for Diffraction Data
Ir	iridium
LL	Lower Limit
MEMS	Microelectromechanical Systems
NIST	National Institute of Standards and Technology
Pb	lead
PCM	Process Control Monitor
Pd	palladium
PM	Process Module
Pt	platinum
PZT	Lead Zirconate Titanate ($\text{PbZr}_x\text{Ti}_{1-x}\text{O}_3$)
PZT(52/48)	PZT with $x = 52$
Si	silicon
SPC	Statistical Process Control
SQI	Silicon Quest International
RC-FWHM	X-ray Diffraction Rocking-Curve Full Width at Half Maximum
TiO_2	titanium dioxide
UL	Upper Limit
XRD	X-ray diffraction

NO. OF COPIES	ORGANIZATION	NO. OF COPIES	ORGANIZATION
1 ELEC	ADMNSTR DEFNS TECHL INFO CTR ATTN DTIC OCP 8725 JOHN J KINGMAN RD STE 0944 FT BELVOIR VA 22060-6218	12	US ARMY RSRCH LAB ATTN IMNE ALC HRR MAIL & RECORDS MGMT ATTN RDRL CIM L TECHL LIB ATTN RDRL CIM P TECHL PUB ATTN RDRL SER L B PIEKARSKI ATTN RDRL SER L B POWER ATTN RDRL SER L D POTREPKA ATTN RDRL SER L G L SMITH ATTN RDRL SER L J MARTIN ATTN RDRL SER L J PULSKAMP ATTN RDRL SER L L SANCHEZ ATTN RDRL SER L R POLCAWICH ATTN RDRL SER P AMIRTHARAJ ADELPHI MD 20783-1197
1 CD	OFC OF THE SECY OF DEFNS ATTN ODDRE (R&AT) THE PENTAGON WASHINGTON DC 20301-3080		
1	US ARMY RSRCH DEV AND ENGRG CMND ARMAMENT RSRCH DEV & ENGRG CTR ARMAMENT ENGRG & TECHNLGY CTR ATTN AMSRD AAR AEF T J MATTS BLDG 305 ABERDEEN PROVING GROUND MD 21005-5001		
1	PM TIMS, PROFILER (MMS-P) AN/TMQ-52 ATTN B GRIFFIES BUILDING 563 FT MONMOUTH NJ 07703		
1	US ARMY INFO SYS ENGRG CMND ATTN AMSEL IE TD A RIVERA FT HUACHUCA AZ 85613-5300		
1	COMMANDER US ARMY RDECOM ATTN AMSRD AMR W C MCCORKLE 5400 FOWLER RD REDSTONE ARSENAL AL 35898-5000		
1	US GOVERNMENT PRINT OFF DEPOSITORY RECEIVING SECTION ATTN MAIL STOP IDAD J TATE 732 NORTH CAPITOL ST NW WASHINGTON DC 20402		
1	US ARMY RSRCH LAB ATTN RDRL CIM G T LANDFRIED BLDG 4600 ABERDEEN PROVING GROUND MD 21005-5066		
			TOTAL: 20 (1 ELEC, 1 CD, 18 HCS)

INTENTIONALLY LEFT BLANK.